The Astronomical Journal, 172:236 (20pp), 2026 October https://doi.org/10.3847/1538-3881/aea160
© 2026. The Author(s). Published by the American Astronomical Society.
OPEN ACCESS

Tracing Radial Migration in the Outer Disk: A Comprehensive Analysis of the Old Open Cluster Berkeley 36

Deniz Cennet Çinar[1], D. Bisht[2], Ing-Guey Jiang[3], K. Belwal[2], and Selçuk Bilir[4]
[1] Programme of Astronomy and Space Sciences, Institute of Graduate Studies in Science, Istanbul University, Istanbul, 34116, Turkey; denizcennetcinar@gmail.com
[2] Indian Centre for Space Physics 466, Barakhola, Singabari Road, Netai Nagar, Kolkata, West Bengal, 700099, India; devendrabisht297@gmail.com
[3] Department of Physics and Institute of Astronomy, National Tsing-Hua University, Hsinchu 30013, Taiwan; jiang@phys.nthu.edu.tw
[4] Istanbul University, Faculty of Science, Department of Astronomy and Space Sciences, 34119, Beyazıt, Istanbul, Turkey
Received 2026 July 30; revised 2026 August 28; accepted 2026 August 29; published 2026 September 28

Abstract

We present a chemo-kinematical, structural, and photometric analysis of the old open cluster Berkeley 36 using Gaia DR3 astrometry and photometry together with high-resolution spectroscopy from the Gaia-ESO Survey DR5.1. Applying a Gaussian mixture model to Gaia astrometry, we identify 946 high-probability cluster members. We derive a core radius of $2\farcm63 \pm 0\farcm21$ and a tidal radius of $14\farcm84 \pm 0\farcm47$, indicating a moderately concentrated and dynamically relaxed system. By fixing the cluster metallicity to the spectroscopic value of $[Fe/H] = -0.19 \pm 0.02$ dex and adopting an independently determined geometric distance of 4377 ± 510 pc, we minimize the classical age–reddening–metallicity degeneracy and derive a robust isochrone age of 6.8 ± 0.5 Gyr. Independent Ba-based chemical clocks yield a mean age of 7.75 ± 1.94 Gyr, supporting the isochrone solution. The cluster exhibits a high main-sequence binary fraction of $48.0\% \pm 1.7\%$ and hosts 83 blue straggler star candidates with an extended spatial distribution, contrary to classical mass segregation. Orbit integration shows that Berkeley 36 follows a nearly circular orbit in the outer Galactic disk ($R_{GC} = 11.42 \pm 0.44$ kpc). Accounting for the Galactic warp and disk flare increases the cluster's maximum vertical excursion by 86% and the local disk scale height by 17%, respectively. Comparison with its chemically inferred birth radius ($R_b = 6.71 \pm 0.66$ kpc) indicates an outward radial migration of approximately 5 kpc, predominantly driven by churning. These results establish Berkeley 36 as a benchmark for investigating radial migration, secular evolution, and the dynamical history of old Galactic open clusters.

Unified Astronomy Thesaurus concepts: Open star clusters (1160); Milky Way disk (1050); Galaxy kinematics (602); Stellar dynamics (1596)

Materials only available in the online version of record: machine-readable table

1. Introduction

Open clusters (OCs) are among the most powerful tracers of the structure, kinematics, and chemical evolution of the Galactic disk. Because their member stars share a common origin, distance, initial chemical composition, and age, OCs provide nearly model-independent anchors for stellar evolutionary theory and serve as benchmarks for the age–metallicity relation (E. D. Friel 1995; C. J. Lada & E. A. Lada 2003; H. Zinnecker & H. W. Yorke 2007; J. D. Kruijssen 2014). Their spatial distribution across Galactocentric radii encodes the present-day metallicity gradient of the disk (e.g., E. D. Friel et al. 2002; H. R. Jacobson et al. 2011; M. Netopil et al. 2016; M. Netopil et al. 2022; Y. C. Joshi et al. 2024), while their age spread, spanning from a few megayears to several gigayears, makes them uniquely suited for reconstructing the star formation history and chemical enrichment of the thin disk over cosmological timescales (L. Magrini et al. 2009; J. Donor et al. 2020).

The launch of the Gaia mission (Gaia Collaboration et al. 2016) has transformed star cluster studies. The high-precision astrometry provided by Gaia DR2, EDR3, and DR3 (Gaia Collaboration et al. 2018, 2021, 2023) has enabled highly reliable membership determination from five-parameter astrometric solutions, greatly reducing the uncertainties of purely photometric methods. Gaia-based all-sky surveys have rediscovered poorly characterized clusters and significantly revised the fundamental parameters of hundreds of known clusters (T. Cantat-Gaudin et al. 2018, 2020; E. L. Hunt & S. Reffert 2024). These homogeneous datasets now provide the basis for Galactic-scale studies of disk structure and evolution (e.g., L. Liu & X. Pang 2019; A. Castro-Ginard et al. 2020; W. S. Dias et al. 2021; O. Plevne & F. Akbaba 2026). Determining accurate fundamental parameters is essential for exploiting the full potential of OCs in studies of stellar evolution and Galactic chemical evolution (E. D. Friel 1995; M. Netopil et al. 2016; M. Netopil et al. 2022; J. M. Otto et al. 2026). However, despite the astrometric advances provided by Gaia, deriving reliable physical properties from photometry alone remains challenging for many OCs.

In traditional color–magnitude diagram (CMD) fitting, age, distance, and reddening are strongly correlated with metallicity (e.g., T. Banks et al. 2020; T. Yontan 2023a; T. Yontan et al. 2023b). Variations in interstellar dust extinction and chemical composition can easily mimic one another along the main sequence (MS), meaning that entirely different parameter combinations can produce nearly identical CMD morphologies (e.g., T. von Hippel et al. 2006; S. Bilir et al. 2010; S. Gokmen et al. 2023; S. Taşdemir & T. Yontan 2023). If all parameters

Original content from this work may be used under the terms of the Creative Commons Attribution 4.0 licence. Any further distribution of this work must maintain attribution to the author(s) and the title of the work, journal citation and DOI.

are left free during isochrone fitting, this well-known degeneracy often leads to nonunique solutions and systematic errors in the derived cluster ages (e.g., Z. F. Bostancı et al. 2015; T. Yontan et al. 2015; T. Ak et al. 2016; D. Bossini et al. 2019; H. Çakmak et al. 2024).

To overcome these photometric limitations and establish a physically consistent profile for Berkeley 36, it is crucial to constrain these variables using independent methods. The combination of Gaia astrometric membership and high-resolution spectroscopy from the Gaia-ESO Survey (GES; G. Gilmore et al. 2022; S. Randich et al. 2022) provides a powerful means of breaking the age–reddening–metallicity degeneracy. GES Data Release 5.1 (DR5.1) provides precise spectroscopic measurements of effective temperatures, surface gravities, and chemical abundances for individual cluster members (A. Hourihane et al. 2023). By securely anchoring the cluster's metallicity with GES data and establishing reliable distances via Gaia, the subsequent isochrone fitting is essentially reduced to a single free parameter: age. By combining independent astrometric and spectroscopic constraints, this approach substantially reduces the inherent degeneracies of photometric analyses and yields more robust cluster parameters (L. Magrini et al. 2017; C. Viscasillas Vázquez et al. 2022).

Accurate cluster parameters not only improve our understanding of stellar evolution but also provide the foundation for investigating the dynamical evolution of the Galactic disk. Galactic disk evolution is shaped not only by star formation and chemical enrichment but also by dynamical processes that redistribute stars over time. Radial migration and orbital blurring mix stellar populations across the disk, complicating efforts to reconstruct the Milky Way's formation history (J. A. Sellwood & J. J. Binney 2002; R. Roškar et al. 2008; I. Minchev et al. 2011). Investigating these processes requires stellar tracers with accurately determined ages, distances, chemical compositions, and kinematics. OCs are ideal because their member stars share a common origin, allowing their fundamental parameters to be determined with high precision. Combined with Gaia astrometry, radial velocities provide full six-dimensional phase-space information, enabling the derivation of Galactic space velocities and orbital parameters (W. S. Dias et al. 2002; C. Soubiran et al. 2018; Z.-Y. Wu et al. 2009; R. Carrera et al. 2019; Y. Tarricq et al. 2021; T. Yontan & R. Canbay 2023c). Orbit integration in realistic Galactic potentials further constrains birth radii, migration histories, and dynamical heating (C. Allen & A. Santillan 1991; A. Irrgang et al. 2013; J. Bovy 2015; F. Anders et al. 2017; L. Spina et al. 2021; C. Viscasillas Vázquez et al. 2022). Consequently, OCs are among the most powerful observational tracers for studying radial migration and blurring, providing key constraints on the formation and evolution of the Galactic disk.

Berkeley 36 ($\alpha_{2000} = 07^{h}17^{m}01^{s}$, $\delta_{2000} = -13°08'48''$; $l = 227.°521$, $b = -0.°412$) is particularly well suited for such a study because it is an intermediate-to-old-age OC located toward the Galactic anticenter, where it serves as a valuable tracer of both the outer-disk metallicity gradient and Galactic dynamical evolution. Previous studies have been largely photometric in nature and limited in scope, providing only preliminary estimates of distance, reddening, and age without the benefit of spectroscopic metallicities or modern astrometric membership (e.g., T. Hasegawa et al. 2004; G. Carraro et al. 2007; A. L. Tadross 2011). Despite recent advances in Gaia-based cluster studies, Berkeley 36 has not yet been investigated using a combined analysis of Gaia astrometry, GES spectroscopy, and TESS photometry, leaving its astrophysical and dynamical properties only partially constrained.

In this paper, we present a comprehensive analysis of Berkeley 36 by combining Gaia DR3 astrometry, GES DR5.1 spectroscopy, and TESS photometry. We determine the cluster's structural and astrophysical parameters through CMD fitting constrained by spectroscopic metallicity, derive its full six-dimensional kinematics from Gaia astrometry and GES radial velocities, and investigate its Galactic orbit and radial migration history using a multicomponent Galactic potential. We also examine the blue straggler and evolved star populations to assess the cluster's dynamical evolutionary state. Together, these analyses provide a comprehensive picture of Berkeley 36, yielding new constraints on its evolutionary history and placing the cluster within the broader framework of Galactic disk formation and evolution.

2. Data

The Gaia space observatory (Gaia Collaboration et al. 2016), conceived and operated under the European Space Agency (ESA), has fundamentally transformed our capacity to construct three-dimensional maps of the Milky Way. Gaia DR3 (Gaia Collaboration et al. 2021) supplies astrometric and photometric measurements for approximately 1.46 billion stellar sources, constituting an unparalleled database for investigations of cluster membership, stellar kinematics, and Galactic structure. The catalog provides, for each source, celestial coordinates (α, δ), trigonometric parallaxes (ϖ), two-dimensional proper-motion vectors ($\mu_\alpha \cos\delta$, μ_δ), and broad-band photometry in the G, G_{BP}, and G_{RP} passbands (M. Riello et al. 2021). This combination of high-precision positional measurements and uniform photometric calibration renders Gaia DR3 particularly well suited for membership determination and CMD studies. We extracted all sources from the Gaia DR3 archive lying within a circular aperture of radius $r = 21'$ centered on the nominal coordinates of Berkeley 36. The query construction and the applied data-quality criteria are documented in Appendix A.

Elemental abundance measurements were drawn from GES DR5.1 (A. Hourihane et al. 2023), which corresponds to the survey's sixth internal data release (iDR6). The spectroscopic data used in this work were obtained from the ESO Science Archive Facility (G. Gilmore & S. Randich 2015). The GES program acquired high-resolution spectra for more than 10^5 stars with the VLT/FLAMES multiobject spectrograph (L. Pasquini et al. 2002) between December 2011 and January 2018. Observations employed both the UVES arm ($R \approx 47{,}000$; gratings U520 and U580, spanning approximately 4140–6840 Å) and the GIRAFFE arm ($R \approx 17{,}000$–$31{,}000$). Stellar atmospheric parameters and individual elemental abundances were derived in a self-consistent manner across all working groups and subsequently placed onto a homogeneous scale through the WG15 homogenization framework described by A. Hourihane et al. (2023). Cluster members identified through our Gaia DR3 membership analysis were cross-matched with the GES catalog using the VizieR XMatch service (T. Boch et al. 2012), adopting a positional tolerance of 1″. This initial cross-match yielded 219 common sources. Following the quality-control recommendations of GES DR5.1, nine stars flagged by the NIA and SRP quality

indicators were excluded, as these correspond to sources with too few spectral lines for reliable abundance determinations.[5] The resulting sample, therefore, comprised 210 stars.

The signal-to-noise ratios (SNRs) of the corresponding spectra span a wide range, from approximately 4–130. To determine an appropriate quality threshold, we examined three SNR limits (SNR $\geqslant$ 20, 25, and 30). Increasing the threshold from 20 to 30 reduces the number of stars with abundance measurements from 106 to 48, while the median metallicity changes only from [Fe/H] $= -0.19$ to -0.18 dex and the median radial velocity varies by less than $\approx$1 km s^{-1} (62.25–61.21 km s^{-1}). Since these variations are negligible compared to the substantial reduction in sample size, we adopted SNR $\geqslant$ 20, thereby maximizing the number of spectroscopic cluster members without introducing a significant systematic bias in the cluster's bulk chemical or kinematic properties. Finally, only stars with available atmospheric parameters and chemical abundance measurements were retained for the subsequent analysis. This resulted in a final spectroscopic sample of 106 stars.

The available atmospheric parameters include the effective temperature ($T_{\rm eff}$), surface gravity ($\log g$), and metallicity ([Fe/H]), together with abundance measurements for a wide range of chemical elements. In the present analysis, we focus on five *s*-process elements, four α-elements, and the odd-*Z* element Na. Elemental abundances are expressed in the standard logarithmic scale, $A({\rm El}) = 12 + \log[n({\rm El})/n({\rm H})]$, while abundances normalized to the solar composition are given by $[{\rm El/H}] = \log[n({\rm El})/n({\rm H})] - \log[n({\rm El})/n({\rm H})]_{\odot}$.

As a preparatory step, a kinematic preselection was applied by retaining only sources whose parallaxes and proper motions lie within 1σ of the cluster mean values reported in E. L. Hunt & S. Reffert (2024). This criterion corresponds to the ranges $-1.864 < \mu_{\alpha}\cos\delta < -1.538$ mas yr^{-1}, $0.806 < \mu_{\delta} < 1.114$ mas yr^{-1}, and $0.102 < \varpi < 0.346$ mas. This preselection substantially reduces field-star contamination before the formal membership analysis. The resulting filtered samples serve as input to the membership procedure detailed in Section 3 and are subsequently used for isochrone fitting, Galactic orbit integration, chemical abundance comparison, and dynamical evolution.

The Transiting Exoplanet Survey Satellite (G. R. Ricker et al. 2015) photometric data used in this work were obtained from the Mikulski Archive for Space Telescopes (MAST) at the Space Telescope Science Institute. The specific TESS observations analyzed in this study, including the light curves of probable Berkeley 36 members and the foreground eclipsing binary candidates, are available via DOI: 10.17909/531f-ks67.

3. Membership Analysis

A robust separation of true cluster stars from the surrounding Galactic disk population is a prerequisite for all subsequent steps in this study. While published Gaia DR3-based membership lists for Berkeley 36 already exist (T. Cantat-Gaudin et al. 2020; E. L. Hunt & S. Reffert 2024), we construct our own catalog so that the sample used throughout this paper is internally uniform and treated with a single, well-defined method. Membership was assigned through a Gaussian mixture model (GMM; A. P. Dempster et al. 1977; G. McLachlan 2000) fitted to the Gaia DR3 proper motions and trigonometric parallaxes of stars projected toward Berkeley 36. In this approach, the observed astrometric distribution is decomposed into two Gaussian components, one tracing the cluster and one tracing the field, and each star is assigned a probability of belonging to the cluster component based on its position in proper-motion/parallax space. Such a probabilistic treatment is particularly well suited to lines of sight where the cluster and disk populations partially overlap kinematically, and it is now routinely applied in OC studies (M. Agarwal et al. 2021; K. Belwal et al. 2025, 2026; D. Bisht et al. 2026a, 2026b).

Working from the Gaia DR3 sources within the adopted search radius, we retained only stars with a full five-parameter astrometric solution and complete photometry across the three Gaia passbands. We further imposed a positive trigonometric parallax ($\varpi > 0$), an upper limit on the proper-motion uncertainty (ϵ_{μ}), and RUWE $\leqslant$ 1.4 (L. Lindegren et al. 2021) to remove sources with unreliable single-star astrometric fits, likely unresolved binaries, or otherwise flawed measurements. Before running the GMM, an approximate cluster locus in ($\mu_{\alpha}\cos\delta$, μ_{δ}, ϖ) space was located with a *k*-nearest neighbors (kNN) search (T. Cover & P. Hart 1967), which was used to initialize the fit and limit early contamination from field stars. The astrometric quantities were standardized, and a two-component GMM was then optimized using the expectation-maximization algorithm, yielding a membership probability P for each star. Stars with $P \geqslant P_{\rm min}$ were retained as probable members, with the threshold chosen to keep the sample as complete as possible while limiting field contamination for Berkeley 36.

With this procedure, we obtain $N_{\rm mem} = 946$ probable members of Berkeley 36 with $P \geqslant 0.7$. The resulting mean proper motion is consistent with previous catalogs (T. Cantat-Gaudin et al. 2020; E. L. Hunt & S. Reffert 2024). A comparison with the membership catalog of E. L. Hunt & S. Reffert (2024) shows substantial agreement between the two samples: of the 678 candidate members identified by E. L. Hunt & S. Reffert (2024), 331 have $P \geqslant 0.7$, all of which are included in our final sample. In addition, 587 stars are common to both catalogs, while the remaining 91 stars identified by E. L. Hunt & S. Reffert (2024) do not meet our adopted membership-probability threshold of $P = 0.7$. Our final catalog contains 946 members, indicating that our selection recovers the high-probability members identified by E. L. Hunt & S. Reffert (2024) while also identifying additional candidate members. As shown in Figure 1, the selected members trace a well-defined spatial and kinematic overdensity, while their parallaxes show a relatively concentrated distribution consistent with the cluster population. Together, these features support the identification of Berkeley 36 as a physically associated stellar group rather than a chance alignment of field stars.

The cluster center was located by finding the position of maximum stellar density on the sky, using the equatorial coordinates of the member stars from Gaia DR3. Separate one-dimensional density profiles were built along α and δ, and each was fitted with a Gaussian function; the peak of each fit was taken as the corresponding coordinate of the density maximum. The resulting central coordinates are $\alpha = 07^{\rm h}16^{\rm m}23.^{\rm s}86$, $\delta = -13^{\circ}11'51.''35$, equivalent to Galactic coordinates $l = 227.^{\circ}496$ and $b = -0.^{\circ}569$ for Berkeley 36. As in similar analyses, the probability cut was set to $P_{\rm min}$=0.7, representing a

[5] https://www.eso.org/rm/api/v1/public/releaseDescriptions/191

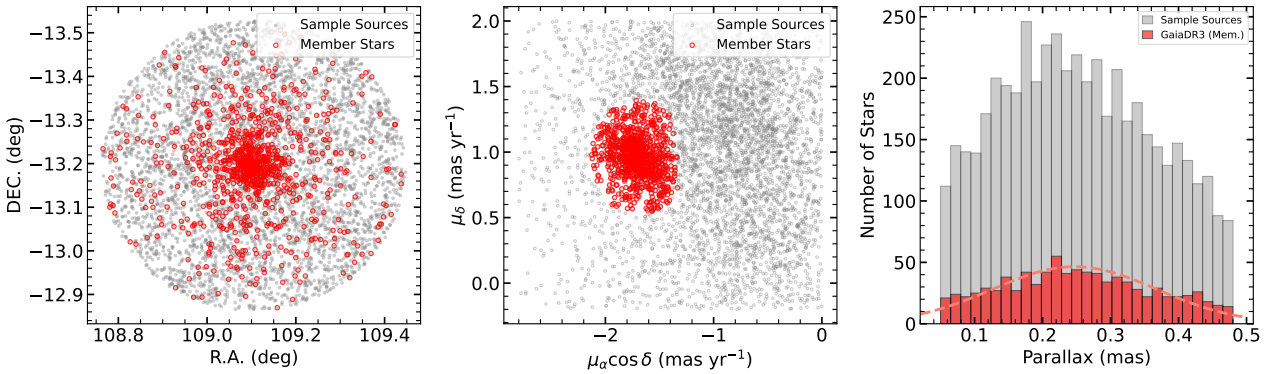


Figure 1. Positional, kinematic, and astrometric properties of Berkeley 36. Left: sky distribution of the surveyed stars in equatorial coordinates (α, δ). Middle: proper-motion vector-point diagram showing the clear offset between the cluster and the field population. Right: trigonometric parallax distribution of the same stars. Gray points and gray bars mark all stars within the searched field, while red circles and red bars indicate the stars retained as probable cluster members from the Gaia DR3 astrometry.

compromise between sample size and purity. We also verified that small changes in this threshold do not significantly affect the derived cluster properties.

The mean astrometric solution for Berkeley 36 was computed from the Gaia DR3 measurements of the adopted member stars. We find a mean proper motion of $\langle \mu_\alpha \cos\delta, \mu_\delta \rangle = (-1.701 \pm 0.163, \quad 0.960 \pm 0.154)$ mas yr^{-1}, while a Gaussian fit to the trigonometric parallax distribution gives $\varpi = 0.224 \pm 0.122$ mas, corresponding to a parallax-based distance of $d_\varpi = 4.46 \pm 2.43$ kpc. These astrometric parameters are consistent with earlier determinations (e.g., T. Cantat-Gaudin et al. 2020; E. L. Hunt & S. Reffert 2024); the full set of derived quantities is listed in Table 1.

4. Structural Parameters Determination

To characterize the cluster's internal structure, we analyzed the radial stellar density distributions of high-probability cluster members identified through our Gaia astrometric analysis. The radial density profile (RDP) was constructed using an equal-area annular binning scheme, ensuring uniform sampling of the stellar density field and comparable Poisson uncertainties across bins, with each annulus containing at least 20 member stars ($N_i \geqslant 20$).

The surface density $\rho(r_i)$ at projected distance r_i from the cluster center was obtained as $\rho(r_i) = N_i/A_i$, where N_i is the star count and A_i the annular area. We fitted the observed profiles with the empirical surface-density model of I. King (1962):

$$\rho(r) = \rho_0 \left[\frac{1}{\sqrt{1 + (r/r_c)^2}} - \frac{1}{\sqrt{1 + (r_t/r_c)^2}} \right]^2 + \rho_{bg}, \quad (1)$$

where ρ_0 is the central density, r_c is the core radius (where $\rho = 0.5\,\rho_0$), r_t is the tidal radius, and ρ_{bg} is the residual background density. Although $\rho_{bg} \approx 0$ is expected for a member-only sample, it was retained as a free parameter to account for residual contamination. Best-fit parameters were estimated by minimizing the negative log-likelihood:

$$\ln \mathcal{L} = -\frac{1}{2} \sum_i \left(\frac{\rho_i - \rho_{i,\mathrm{model}}}{\sigma_{\rho_i}} \right)^2, \quad (2)$$

where σ_{ρ_i} is the Poisson uncertainty in each annulus.

Parameter optimization was performed using the MCMC ensemble sampler `emcee` (D. Foreman-Mackey et al. 2013) with 100 walkers, 5000 steps, and a 500-step burn-in, adopting broad uniform priors on all parameters. Chain convergence was confirmed via the A. Gelman & D. B. Rubin (1992) $\hat{R}$ diagnostic ($\hat{R} < 1.1$). The resulting best-fit model and 1σ confidence interval are shown in the upper panel of Figure 2, while the posterior distributions of the fitted parameters are shown in the lower-corner plot. The narrow posterior distributions demonstrate that the structural parameters are tightly constrained despite the cluster's large distance. The structural parameters are summarized in Table 1.

For Berkeley 36, the MCMC analysis yields a central density $\rho_0 = 15.10^{+1.50}_{-1.38}$, a core radius $r_c = 2.63^{+0.22}_{-0.21}$ arcmin, a tidal radius $r_t = 14.84^{+0.47}_{-0.47}$ arcmin, and a background density $\rho_{bg} = 0.22^{+0.01}_{-0.01}$. All posterior distributions are well constrained and approximately unimodal, and the low correlation among r_t, r_c, and ρ_{bg} indicates that the fit is robust, with the only appreciable degeneracy occurring between ρ_0 and r_c, as expected from the functional form of the King profile.

Following I. King (1962), the concentration parameter $C = \log(r_t/r_c)$ indicates a cluster's physical compactness and dynamical state. For Berkeley 36, we obtain $C \approx 0.75$ ($r_t/r_c \approx 5.6$), a value comparable to those typically found for moderately concentrated, dynamically relaxed OCs, and consistent with an evolved system that has undergone significant two-body relaxation.

5. Color–Magnitude Diagram and Fundamental Parameters

Accurate fundamental parameters such as reddening, distance, metallicity, and age are prerequisites for interpreting the formation history and dynamical state of OCs and for tracing the chemical and structural evolution of the Galactic disk (E. D. Friel 1995; M. Netopil et al. 2016). However, their derivation from CMD analysis is nontrivial. Clusters at low Galactic latitudes suffer from substantial interstellar extinction and spatially variable reddening (G. Burki 1975; G. Carraro et al. 2017), while the OC population itself spans a broad metallicity range, with cluster-to-cluster differences reaching ~0.25 dex (D. C. Çınar et al. 2024; S. Taşdemir et al. 2026). Compounding these difficulties, reddening, distance modulus, metallicity, and age are mutually correlated in isochrone space (S. Bilir et al. 2006a, 2010; T. von Hippel et al. 2006;

Table 1
Derived Physical and Kinematic Parameters of Berkeley 36

Parameter	Symbol	This Study
Astrometric Parameters		
Right ascension	α (hh:mm:ss)	07:16:23.86
Decl.	δ (dd:mm:ss)	−13:11:51.35
Galactic longitude	l (degree)	227.496
Galactic latitude	b (degree)	−0.569
Mean proper motion (RA)	$\langle \mu_\alpha \cos\delta \rangle$ (mas yr^{-1})	-1.701 ± 0.163
Mean proper motion (Dec)	$\langle \mu_\delta \rangle$ (mas yr^{-1})	0.960 ± 0.154
Mean trigonometric parallax	$\langle \varpi \rangle$ (mas)	0.224 ± 0.122
Mean parallax distance	$\langle d_\varpi \rangle$ (kpc)	4.46 ± 2.43
Structural Parameters		
Central surface density	ρ_0 (stars arcmin^{-2})	$15.10^{+1.50}_{-1.38}$
Background density	$\rho_{\rm bg}$ (stars arcmin^{-2})	$0.22^{+0.01}_{-0.01}$
Core radius	$r_{\rm c}$ (arcmin)	$2.63^{+0.22}_{-0.21}$
Tidal radius	$r_{\rm t}$ (arcmin)	$14.84^{+0.47}_{-0.47}$
Concentration parameter	C	$0.75^{+0.05}_{-0.05}$
Fundamental Parameters		
Geometric distance	$\langle d_{\rm geo} \rangle$ (pc)	4377 ± 510
True distance modulus	$(m-M)_0$ (mag)	13.206 ± 0.253
Apparent distance modulus	$(m-M)$ (mag)	14.800 ± 0.379
V-band extinction	$\langle A_{\rm V} \rangle$ (mag)	1.594 ± 0.283
Color excess (UBV)	$E(B-V)$ (mag)	0.514 ± 0.091
Color excess (Gaia)	$E(G_{\rm BP}-G_{\rm RP})$ (mag)	0.725 ± 0.129
G-band extinction	$\langle A_{\rm G} \rangle$ (mag)	1.350 ± 0.045
Iron abundance	[Fe/H] (dex)	-0.19 ± 0.02
Metallicity	Z	0.01001 ± 0.0004
Age (isochrone)	$t_{\rm iso}$ (Gyr)	6.8 ± 0.5
Age (chemical clock)	$t_{\rm [Ba/X]}$ (Gyr)	7.75 ± 1.94
Galactic Orbital Parameters		
Radial velocity	$\langle V_{\rm rad,OC} \rangle$ (km s^{-1})	62.80 ± 0.04
Perigalactic radius	$R_{\rm peri}$ (kpc)	11.369 ± 0.437
Apogalactic radius	$R_{\rm apo}$ (kpc)	12.214 ± 1.139
Mean orbital radius	$R_{\rm m}$ (kpc)	11.791 ± 0.610
Orbital eccentricity	e	0.036 ± 0.027
Maximum vertical height	$Z_{\rm max}$ (kpc)	0.380 ± 0.023
Present Galactocentric radius	$R_{\rm GC}$ (kpc)	11.422 ± 0.437
Guiding radius	$R_{\rm g}$ (kpc)	11.751 ± 0.772
Chemical birth radius	$R_{\rm b}$ (kpc)	6.71 ± 0.66
Orbital period	$T_{\rm p}$ (Myr)	345 ± 26
Space Velocities		
Velocity component	$U_{\rm LSR}$ (km s^{-1})	-58.56 ± 3.79
Velocity component	$V_{\rm LSR}$ (km s^{-1})	-8.93 ± 3.40
Velocity component	$W_{\rm LSR}$ (km s^{-1})	-15.98 ± 2.03
Space velocity	$S_{\rm LSR}$ (km s^{-1})	61.36 ± 5.48

G. Andreuzzi et al. 2011; B. Akbulut et al. 2021; S. Koç et al. 2022; T. Yontan et al. 2026), so that unconstrained simultaneous fitting can yield degenerate or physically inconsistent solutions (S. Bilir et al. 2016; Z. F. Bostancı et al. 2018; T. Yontan et al. 2019, 2022; H. Karagöz et al. 2025; B. Tanık Öztürk et al. 2025). To mitigate these degeneracies in our analysis of Berkeley 36, we adopted a sequential parameter-fixation strategy. Line-of-sight extinction was estimated on a star-by-star basis from the three-dimensional dust maps of G. M. Green et al. (2019), providing a spatially resolved treatment of reddening across the cluster

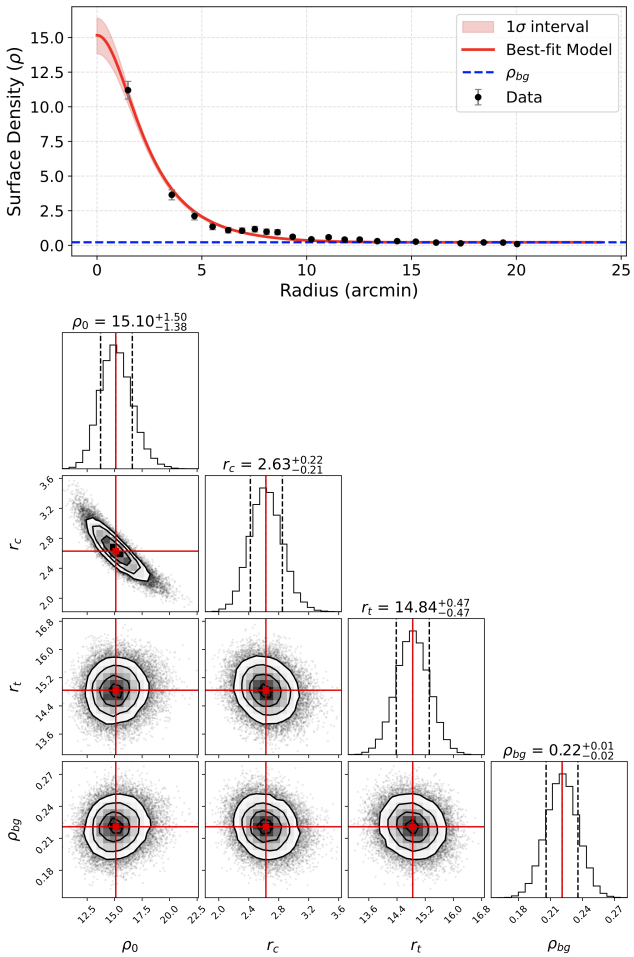


Figure 2. RDP and MCMC posterior distributions for Berkeley 36. Upper panel: observed surface density (ρ) as a function of radial distance from the cluster center (black points with Poisson error bars). The solid red curve is the best-fitting I. King (1962) model, with the shaded region indicating the 1σ confidence interval. The horizontal blue dashed line marks the background density level ($\rho_{\rm bg}$). Lower panels: corner plot of the posterior distributions for the fitted King model parameters (ρ_0, $r_{\rm c}$, $r_{\rm t}$, $\rho_{\rm bg}$), with median values (solid red lines) and 1σ boundaries (dashed lines).

field. Individual stellar distances were drawn from the Bayesian photogeometric catalog of C. A. L. Bailer-Jones et al. (2021), which combines Gaia trigonometric parallaxes with photometric priors to yield reliable distance estimates for Berkeley 36. Metallicity was anchored to the value derived from high-resolution GES spectroscopy. With reddening, distance, and metallicity independently constrained, the CMD fit reduces to a single free parameter, cluster age, thereby yielding more robust, uniquely determined results than a fully free isochrone fit.

5.1. Geometric Distance

One of the key advantages of the Gaia mission is the ability to determine stellar distances directly through trigonometric parallax measurements. However, the accuracy of this method decreases significantly beyond approximately 2 kpc from the Sun, where increasing relative uncertainties in parallax measurements and reduced signal-to-noise ratios limit its reliability (O. Plevne et al. 2020; S. Döner et al. 2023). In this regime, directly inverting observed parallaxes can yield biased and physically inconsistent distance estimates, necessitating

statistical corrections for robust applications. Given that Berkeley 36 is located at a distance of approximately 3.5 kpc, using raw parallax values for individual cluster members is inappropriate. Instead, we adopt the Bayesian geometric distance estimates of C. A. L. Bailer-Jones et al. (2021), which incorporate parallax measurements within a probabilistic framework. This method also accounts for prior assumptions about the spatial distribution of stars in the Galaxy, thereby providing more stable and reliable distance estimates, particularly for distant and low-precision parallax sources. The adoption of these Bayesian distances plays a crucial role in reducing parameter degeneracies in the subsequent cluster analysis.

In this context, individual distances for the cluster members were adopted from the catalog of C. A. L. Bailer-Jones et al. (2021), who derived Bayesian distance estimates for approximately 1.47 billion Gaia EDR3 sources. This catalog combines trigonometric parallax measurements with a direction-dependent prior based on a three-dimensional model of the Milky Way. It provides two types of distance estimates for each source: the purely geometric distance ($d_{\rm geo}$), which relies predominantly on trigonometric parallax, and the photogeometric distance ($d_{\rm pgeo}$), which additionally incorporates photometric information such as stellar magnitudes and color indices. In this study, we adopt $d_{\rm geo}$ because it relies solely on trigonometric parallax and the astrometric prior, without being influenced by photometric information that may introduce additional systematics for cluster members with uncertain or blended photometry. For each source, C. A. L. Bailer-Jones et al. (2021) additionally provides the 16th and 84th percentiles of the posterior distance distribution, which we adopt as the lower and upper 1σ uncertainty bounds on the individual distance estimates.

Because the membership catalog does not include Gaia EDR3 source identifiers, the cluster members were matched with the catalog of C. A. L. Bailer-Jones et al. (2021) using their sky coordinates. For this purpose, a cone search around the cluster field was performed using the VizieR service, and the sources were cross-matched within a $1''$ radius, consistent with Gaia's astrometric precision. Only confirmed cluster members were retained in the final sample. The median geometric distance of the cluster members, together with the 16th and 84th percentiles of the distribution, was $d_{\rm geo} = 4377 \pm 510$ pc. This result confirms Berkeley 36 as a distant OC located well beyond the solar neighborhood.

5.2. Interstellar Extinction

Accurate OC parameters are strongly hampered by interstellar reddening, which is tightly coupled to both distance and age when fitting isochrones. Properly accounting for interstellar extinction is therefore a prerequisite for breaking the degeneracies that otherwise arise among the photometric parameters. Rather than assuming a single, cluster-wide extinction value, we exploit a three-dimensional, distance-resolved reddening approach in which line-of-sight extinction is estimated individually for each member star. This is achieved by combining the precise photogeometric distances obtained in Section 5.1 with a Galactic dust model, yielding a spatially resolved treatment of reddening across the cluster field.

We derived the line-of-sight reddening of the cluster members from the three-dimensional BAYESTAR19 dust map

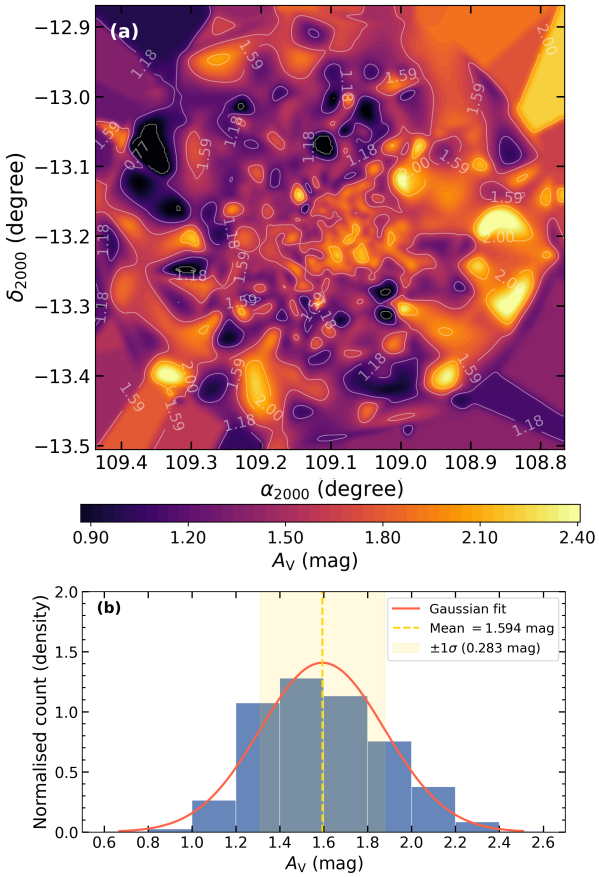


Figure 3. Interstellar extinction properties of the Berkeley 36 member stars. (a) Spatial distribution of A_V across the cluster field, reconstructed from the BAYESTAR19 dust model (G. M. Green et al. 2019); the contours and color scale trace the extinction level. (b) Distribution of individual A_V values, with the red curve showing the Gaussian fit, the vertical dashed line marking the mean, and the shaded band indicating the $\pm 1\sigma$ range.

of G. M. Green et al. (2019), which is calibrated following E. F. Schlafly & D. P. Finkbeiner (2011) and combines Pan-STARRS 1 and 2MASS photometry to yield distance-dependent extinction estimates that are broadly compatible with Gaia astrometry. For each member, the reddening was interpolated at the star's sky position and geometric distance ($d_{\rm geo}$); to suppress the effect of small-scale dust inhomogeneities, we adopted the median of the interpolated posterior as the representative value for that star. Since BAYESTAR19 reports reddening in the Gaia photometric system, we converted the native $E(G_{\rm BP} - G_{\rm RP})$ values to the Johnson–Cousins system via $E(G_{\rm BP} - G_{\rm RP}) = 1.41 \times E(B - V)$ and $A_{\rm G} = 0.83627 \times A_V$ (R. Canbay et al. 2023), and obtained the visual extinction from $A_V = 3.1 \times E(B - V)$ (J. A. Cardelli et al. 1989).

Figure 3(a) shows the extinction field toward Berkeley 36, constructed by interpolating the individual A_V estimates of member stars onto a regular spatial grid. The resulting map reveals clear evidence of differential reddening: extinction is not uniformly distributed across the field but instead traces the underlying dust structure, with localized patches reaching $A_V \sim 2.4$ mag while the bulk of the cluster area shows comparatively lower values around the cluster median. The corresponding histogram of individual member extinctions (Figure 3(b)) is well approximated by a single Gaussian

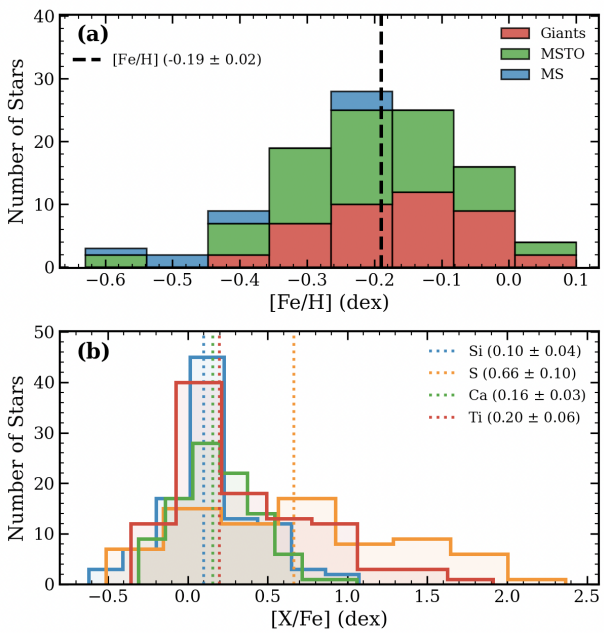


Figure 4. Chemical abundance distributions of Berkeley 36 member stars with SNR $\geqslant$20 from GES data. Panel (a): [Fe/H] distribution, with bin colors indicating stellar evolutionary stage. Panel (b): abundance distributions of Si, S, Ca, and Ti. Dotted vertical lines mark the median of each distribution, with uncertainties given as the standard error of the median.

component, with no evidence for multiple reddening populations or strong asymmetry, consistent with the closeness of the mean (1.594 mag) and median (1.571 mag) values of the sample. This near-symmetric behavior points to a foreground dust screen that varies smoothly on the cluster's angular scale rather than being dominated by compact, high-density clumps.

Among the 946 member stars with reliable dust-map estimates, the mean reddening is $\langle E(B-V)\rangle = 0.514 \pm 0.091$ mag, corresponding to a mean V-band extinction of $\langle A_V\rangle = 1.594 \pm 0.283$ mag. The equivalent extinction in the Gaia photometric system is $E(G_{BP} - G_{RP}) = 0.725 \pm 0.129$ mag and $A_G = 1.350 \pm 0.045$ mag. The substantially higher reddening derived for Berkeley 36, compared to typical nearby OCs, reflects its location in a heavily obscured region of the Galactic disk.

5.3. Metallicity

Spectroscopic [Fe/H] and [α/Fe] abundances for Berkeley 36 were taken from the GES DR5.1 catalog (A. Hourihane et al. 2023), which offers a solid basis for both isochrone selection and chemical characterization (R. Carrera & E. Pancino 2011). Applying an SNR $\geqslant$20 quality cut to the high-probability cluster members yielded a final sample of 106 stars with 319 individual spectra, covering $13.8 < G\,(\mathrm{mag}) \leqslant 18.5$ and concentrated mainly along the MS and MSTO regions of the CMD; further details of the sample selection are provided in Section 2.

As shown in Figure 4(a), the stars with measured iron abundances are distributed predominantly along the giant branch, with a smaller number located around the MSTO and MS regions. The individual [Fe/H] measurements obtained from the Gaia-ESO Survey spectra for the 106 stars span roughly $-0.7 <$ [Fe/H] (dex) $\leqslant +0.2$ dex. This relatively broad observed range should not be interpreted as the intrinsic metallicity dispersion of Berkeley 36, as the sample includes stars at different evolutionary stages and individual spectroscopic measurements naturally carry different uncertainties. Open clusters are generally expected to exhibit relatively small intrinsic metallicity dispersions (e.g., J. Bovy 2016; A. Sinha et al. 2024); therefore, the observed spread is more appropriately regarded as reflecting the combined effects of measurement uncertainties and the heterogeneous evolutionary stages represented in the spectroscopic sample. The distribution is centered around $\langle [Fe/H]\rangle = -0.19 \pm 0.02$ dex, which we adopt as the representative metallicity of Berkeley 36.

Not every α element has uniform spectral-line coverage in the literature, so the analysis was restricted to O, Mg, Si, S, Ca, and Ti. All 106 stars in our spectroscopic sample have reliable [Fe/H] measurements, whereas α-element measurements are not available for every star. Consequently, the number of stars with available measurements varies among the individual elements: 6, 6, 102, 75, 98, and 102 for O, Mg, Si, S, Ca, and Ti, respectively. The resulting median ratios are [O/Fe] =0.23 $\pm$ 0.03, [Mg/Fe] =0.03 $\pm$ 0.05, [Si/Fe] =0.10 $\pm$ 0.04, [S/Fe] =0.66 $\pm$ 0.10, [Ca/Fe] =0.16 $\pm$ 0.03, and [Ti/Fe] =0.20 $\pm$ 0.06 dex, corresponding to a weighted mean [α/Fe] = 0.17 $\pm$ 0.02 dex (Figure 4(b)). We note that the O and Mg ratios rest on only six member stars each and should therefore be regarded as tentative, whereas the Si, Ca, and Ti abundances are based on considerably larger samples and provide more reliable estimates of the α-element abundance pattern. The unusually broad [S/Fe] distribution should be treated with caution. The enhanced O, Ca, and Ti abundances indicate that the chemical enrichment of Berkeley 36 was primarily driven by core-collapse (Type II) supernovae, which dominate the production of α-elements in the early stages of Galactic chemical evolution (A. McWilliam 1997; C. Kobayashi et al. 2006; K. Nomoto et al. 2013). The varying enhancement levels among the individual α-elements likely reflect the metallicity- and progenitor-mass-dependent nucleosynthetic yields of massive stars, as predicted by theoretical supernova models (S. E. Woosley & T. A. Weaver 1995; C. Kobayashi et al. 2006, 2020). We do not interpret the sulfur abundance as evidence for a distinct enrichment pattern because of the unusually large observed scatter in [S/Fe].

The comparatively large [S/Fe] =0.66 $\pm$ 0.10 dex value, based on 75 member stars, should be treated with caution. The [S/Fe] distribution exhibits an unusually large scatter, extending over nearly 3 dex, which is substantially larger than the intrinsic abundance dispersions typically expected for open clusters (e.g., J. Bovy 2016; A. Sinha et al. 2024). We therefore do not consider the sulfur measurements sufficiently reliable for drawing conclusions about the chemical properties or enrichment history of Berkeley 36.

To place this measurement on the scale required by the stellar evolution models (e.g., D. C. Çınar et al. 2024, 2025, 2026c; A. Y. Alzhrani et al. 2025a, 2025b; W. H. Elsanhoury et al. 2025, 2026), the mean iron abundance $\langle$[Fe/H]$\rangle = -0.19 \pm 0.02$ dex was converted to a heavy-element mass fraction using the calibrated relation (e.g., S. Taşdemir et al. 2025; S. Bilir et al. 2026; D. Bisht et al. 2026b, 2026c; R. Canbay et al. 2026):

$$Z_x = \frac{Z}{0.7515 - 2.78 \times Z} \tag{3}$$

$$[\mathrm{Fe/H}] = \log(Z_x) - \log\left(\frac{Z_\odot}{1 - 0.248 - 2.78 \times Z_\odot}\right), \tag{4}$$

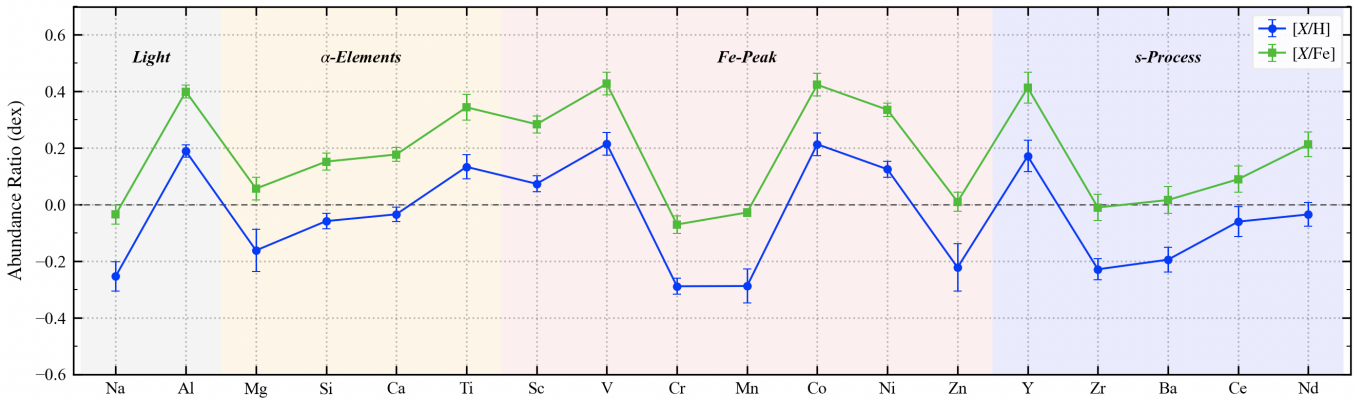


Figure 5. Elemental abundance pattern of Berkeley 36 derived from member stars with high-resolution spectroscopy. Blue circles show [X/H] and green squares show [X/Fe] ratios (in dex) for each element, with error bars representing the associated uncertainties. Elements are grouped into four categories, indicated by the shaded background regions and labels: light elements (Na, Al), α-elements (Mg, Si, Ca, Ti), Fe-peak elements (Sc, V, Cr, Mn, Co, Ni, Zn), and *s*-process elements (Y, Zr, Ba, Ce, Nd). The dashed horizontal line marks the solar abundance ratio.

with $Z_{\odot} = 0.0152$, giving $Z = 0.01001 \pm 0.0004$, which is adopted in the subsequent isochrone fitting.

Figure 5 presents the elemental abundance pattern of Berkeley 36, showing both [X/H] and [X/Fe] ratios for a set of light, α-, Fe-peak, and *s*-process elements. The light elements Na and Al display distinct behavior: while [Na/H] is slightly subsolar, [Al/Fe] shows a clear enhancement of $\sim +0.4$ dex, consistent with the well-known Na-Al abundance trends observed in evolved cluster giants. Among the α-elements (Mg, Si, Ca, Ti), the [X/Fe] ratios are all mildly enhanced relative to solar, ranging from $\sim +0.05$ to $+0.35$ dex, a pattern typical of an old, moderately metal-poor OC whose stars formed before significant enrichment by Type Ia supernovae. The Fe-peak elements exhibit more scatter: Sc, V, Co, and Ni are all enhanced in [X/Fe] by $+0.3$ to $+0.4$ dex, whereas Cr and Mn remain close to the solar value, and Zn is essentially solar within the uncertainties. This dichotomy likely reflects the differing nucleosynthetic origins of these species, since Sc, V, Co, and Ni are produced primarily in core-collapse supernovae (Type II), while Cr and Mn are more closely tied to Type Ia events. Finally, the *s*-process elements show a mixed picture: Y is enhanced by $\sim +0.4$ dex in [Y/Fe], while Zr, Ba, Ce, and Nd remain close to the solar ratio, suggesting only a modest contribution from asymptotic giant branch (AGB) nucleosynthesis to the present-day chemical inventory of the cluster. Overall, the abundance pattern of Berkeley 36 is broadly consistent with that expected for an old Galactic disk OC, exhibiting generally enhanced α-element abundances and no evidence for anomalous *s*-process enrichment (e.g., A. Bragaglia et al. 2008; L. Magrini et al. 2017; A. Bragaglia et al. 2018).

5.4. Isochrone Fitting

CMDs remain one of the most powerful diagnostics for recovering the fundamental parameters of star clusters, since the loci traced by genuine members can be directly compared with theoretical stellar evolutionary tracks (e.g., R. Carrera & E. Pancino 2011). The left panel of Figure 6 shows the G versus $G_{BP} - G_{RP}$ diagram of Berkeley 36, built exclusively from the high-probability members recovered in our astrometric membership analysis. The resulting sequence is well populated from the MS up through the MSTO and continues into the RGB and red clump region. As a consistency check, we compared our astrometrically selected members against independent catalogs from the literature, namely the list of relevant catalogs used for the Berkeley 36 cross-match, (e.g, V. V. Jadhav & A. Subramaniam 2021; A. Hourihane et al. 2023; E. L. Hunt & S. Reffert 2024). The sequences obtained from our own selection agree closely with these external samples across the full magnitude range probed, supporting the reliability of the adopted membership criteria.

Before the isochrone comparison, the basic cluster parameters entering the CMD analysis were fixed using independent methods: metallicity from spectroscopy, and reddening and distance from photometric/astrometric data. For Berkeley 36, we adopted a heliocentric distance of $\langle d \rangle = 4377 \pm 510$ pc, a Gaia G-band extinction of $\langle A_G \rangle = 1.350 \pm 0.045$ mag, and a metallicity of $\langle [Fe/H] \rangle = -0.19 \pm 0.02$ dex. With these quantities held fixed, the cluster's age was then constrained by matching the observed CMD morphology to theoretical isochrones.

We tested the observed sequences against two independent sets of theoretical isochrones, PARSEC CMD 3.9[6] (A. Bressan et al. 2012) and MIST v2.5[7] (J. Choi et al. 2016; A. Dotter 2016), both evaluated at the spectroscopic metallicity quoted above. For the MIST grid, we assumed a rotation rate of $v/v_{crit} = 0$ and considered α-enhancement values of $[\alpha/Fe] = 0.0$ and/or 0.2 dex. The MIST turnoff falls at slightly bluer colors relative to PARSEC, a difference attributable to small physical differences between the two model sets (solar calibration, rotational mixing, convective overshoot); comparable offsets have been reported for other clusters (N. Bastian et al. 2025). Changing the α-element abundance in the MIST grid affects the fitted CMD, indicating that the age solution is not sensitive to the assumed α-enhancement over the range tested. The best-fitting isochrones give an age of 6.8 ± 0.5 Gyr for Berkeley 36, with the MS, MSTO, and RGB simultaneously reproduced within the quoted uncertainties by both model grids.

5.5. Binary Fraction

The fraction of binary systems in an OC carries useful information about its dynamical history, internal kinematics,

[6] https://stev.oapd.inaf.it/cgi-bin/cmd
[7] https://mist.science/interp_isos.html

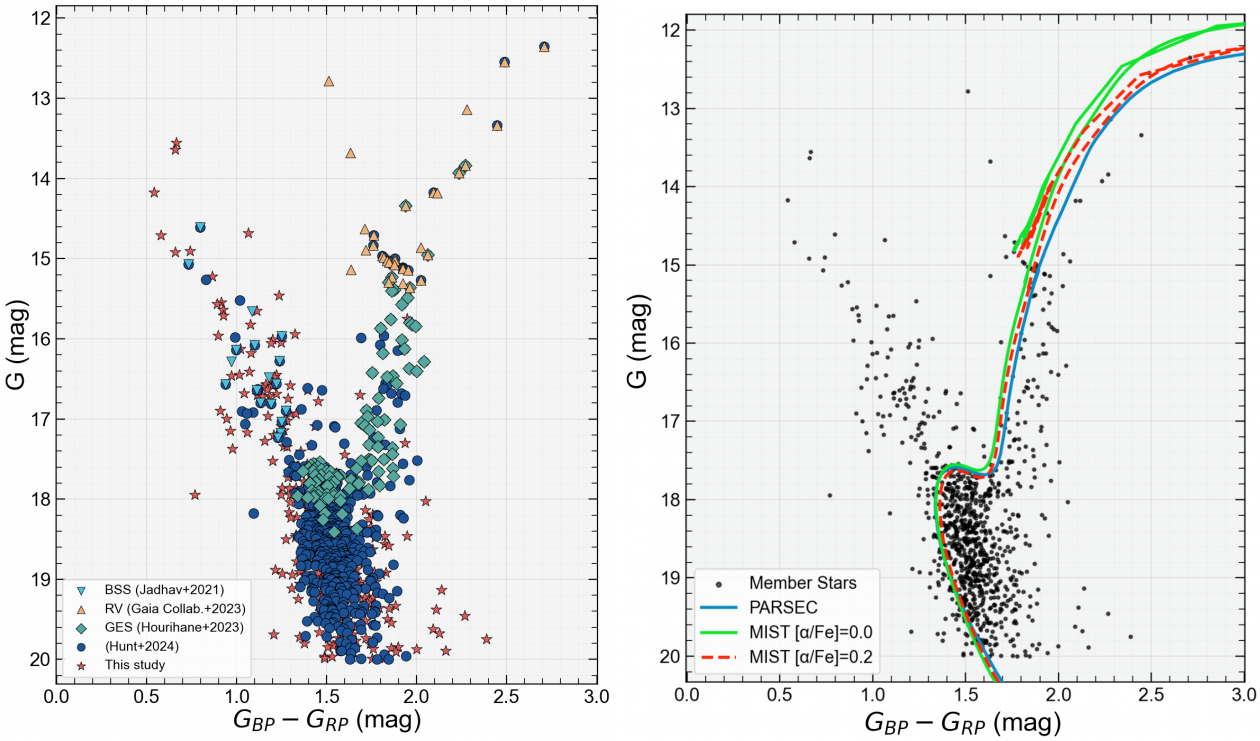


Figure 6. Members are color coded according to the cross-matched literature catalogs, as indicated in the legend (left panel). CMDs of the high-probability cluster members. In the right panel, cluster members are shown as black points. The solid curves represent the best-fitting theoretical PARSEC (blue) and MIST (green and red) isochrones.

and long-term stability (e.g., T. von Hippel et al. 2002; A. Sollima et al. 2007). Because unresolved binaries can shift and broaden the main sequence in a CMD, ignoring them can lead to biased estimates of a cluster's stellar population (A. P. Milone et al. 2012). Following the photometric approach described by A. P. Milone et al. (2012) and J. Donada et al. (2023), we examined the binary content of Berkeley 36.

Main-sequence stars were selected from the turnoff magnitude ($G_{\rm MSTO} = 18$ mag) down to four magnitudes fainter. This selection yielded a sample of 337 MS stars. A fourth-degree polynomial was fitted to the median ridge line of this sample to represent the single-star sequence. To reduce the impact of differential reddening, all magnitudes and color indices were first corrected for extinction, using the cluster's distance modulus and mean reddening (Table 1), so that the fit was performed in the dereddened $(G_{\rm BP} - G_{\rm RP})_0$ versus $M_{\rm G}$ CMD.

The magnitude difference between an unresolved binary and a single star of the same mass was estimated from $\Delta m = -2.5\log_{10}(1 + q^{\alpha})$ with the mass–luminosity index fixed at $\alpha = 3.5$, appropriate for main-sequence stars (Z. Eker et al. 2015, 2018, 2024), and $q = M_2/M_1$ the mass ratio of the two components. For $q = 0.5$, this yields $\Delta m \approx -0.107$ mag, which we adopted as the minimum magnitude offset for classifying a star as a binary candidate, that is, any star lying more than 0.107 mag above the single-star ridge line.

Figure 7(a) shows the resulting CMD, with the fitted single-star locus and the two selection boundaries overplotted. The bulk of the sample follows the main-sequence fit closely, but a second, fainter-in-offset sequence running parallel and above it is clearly visible, as expected for a population of unresolved binaries; the scatter widens toward fainter magnitudes as photometric errors grow. Figure 7(b) shows the corresponding ΔG histogram, spanning −3.075–2.328 mag with a median of −0.314 mag; most stars cluster near the single-star locus, but a distinct secondary excess appears beyond the adopted Δm threshold. The cumulative ΔG distribution in Figure 7(c) marks the region between the two boundaries used to isolate binary candidates.

Out of 337 MS stars, 165 fall within the binary-candidate region, corresponding to a binary fraction of $f_{\rm b} = 0.480 \pm 0.017$ (68% confidence interval: 0.463, 0.497). This is consistent, within uncertainties, with the binary fraction we derived for Berkeley 32 and with values reported for other old OCs analyzed with comparable techniques (e.g., A. P. Milone et al. 2012; J. Donada et al. 2023; D. C. Çınar et al. 2026a).

Splitting the binary candidates by mass ratio, we find 15 systems with $0.5 \leqslant q \leqslant 0.6$, 30 with $0.6 < q \leqslant 0.7$, 49 with $0.7 < q \leqslant 0.8$, 57 with $0.8 < q \leqslant 0.9$, and 14 with $0.9 < q \leqslant 1$. As with Berkeley 32, the distribution is not flat: it rises steadily from low q to a clear maximum in the 0.8–0.9 bin, with the next-highest bin (0.7–0.8) also well populated, before dropping sharply near $q \sim 1$. The concentration near $q \sim 0.8$–0.9 is consistent with the pile-up expected for detached binaries, while the broader shoulder extending down to $q \sim 0.7$ may include a mix of semidetached, contact, or otherwise interacting systems rather than a single well-defined population (e.g., S. Bilir et al. 2005; O. Demircan et al. 2006; Z. Eker et al. 2006; C. Ibanoğlu et al. 2006; Z. Eker et al. 2014). Spectroscopic confirmation would be needed to disentangle these subpopulations. Overall, the mass-ratio distribution in Berkeley 36 mirrors that found for Berkeley 32, suggesting that similar dynamical processes shape the binary population in both clusters despite differences in age or metallicity. As before, since our method loses sensitivity below $q \approx 0.5$, the

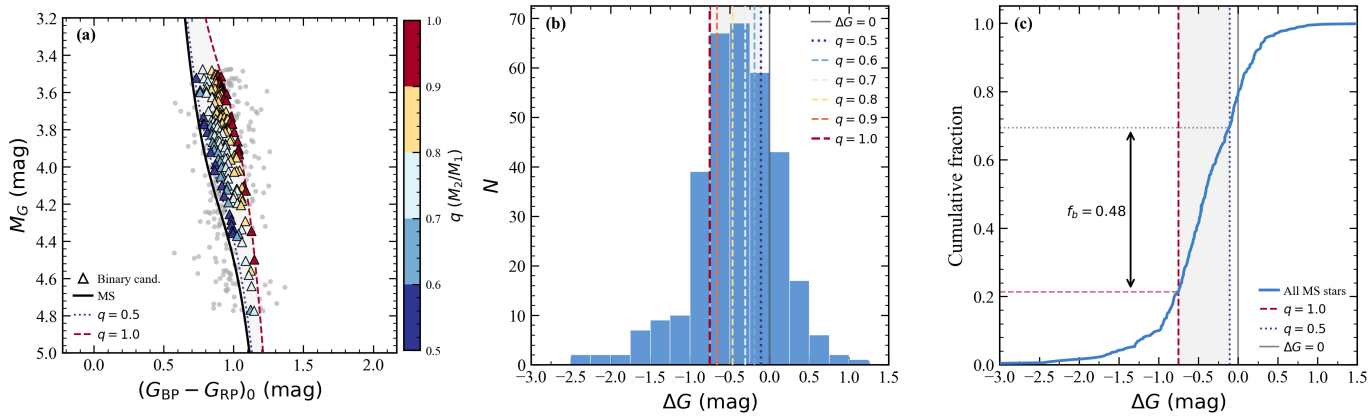


Figure 7. Binary fraction analysis of Berkeley 36. (a) CMD of the MS stars. The solid line shows the fitted single-star sequence; the dashed and dotted lines mark the lower and upper limits of the binary selection region, respectively. Triangle symbols indicate binary candidates. (b) Distribution of ΔG residuals. The shaded region denotes the binary selection zone between the lower and upper limits. (c) Cumulative distribution of ΔG. The binary fraction f_b is indicated by the vertical arrow spanning the two selection limits.

quoted binary fraction should be taken as a lower limit on the cluster's true binary content.

5.6. Blue and Yellow Straggler Stars

We also investigated the Blue Straggler Star (BSS) and Yellow Straggler Star (YSS) populations of Berkeley 36 using cluster members with membership probabilities greater than 70%. As expected for an old and dynamically evolved OC, Berkeley 36 exhibits a noticeable BSS population (E. Linck & R. D. Mathieu 2026).

BSS occupy a well-defined region of the CMD, lying blueward and brighter than the cluster MSTO but still consistent with core hydrogen burning, since they are understood to be the products of mass transfer, mergers, or stellar collisions within binary systems (W. H. McCrea 1964; P. J. T. Leonard 1989; N. Andronov et al. 2006). Following the approach adopted by V. V. Jadhav & A. Subramaniam (2021) and E. Linck & R. D. Mathieu (2026), we defined the boundaries of the BSS region in the CMD using the zero-age main sequence (ZAMS) and the terminal-age main sequence (TAMS), computed from PARSEC isochrones at the cluster age, metallicity, distance modulus, and mean extinction listed in Table 1. The ZAMS marks the blue (bluest, unevolved) edge of the region, corresponding to the locus of stars that have just begun hydrogen burning, while the TAMS marks its red edge, corresponding to the reddest colors a star can reach while still on the main sequence before evolving toward the subgiant branch. Together, the ZAMS and TAMS define the full width in color that a genuine MS star can occupy at any given magnitude; a star located blueward of this band, and brighter than the MSTO, cannot be explained by single-star evolution and is therefore flagged as a BSS candidate. We additionally overlaid the equal-mass binary sequence, obtained by shifting the isochrone brighter by -0.753 mag (for $q = 1$) to help distinguish genuine BSS from unresolved near-equal-mass binaries of normal MS stars that can mimic a similar CMD position.

YSS candidates were identified following the same methodology, as stars lying just redward of the TAMS boundary and above the base of the giant branch—a region populated by BSS that have started to evolve off the main sequence and cool toward the giant branch while retaining an anomalously high luminosity for their color, as discussed by E. Linck & R. D. Mathieu (2026).

To identify previously reported BSS candidates, we cross-matched our member sample with the catalog of V. V. Jadhav & A. Subramaniam (2021), recovering 18 stars in common. Applying the CMD criteria described above, we identified 10 YSS candidates. In addition to the literature-confirmed sources, we identified 65 new photometric BSS candidates from their positions in the CMD, as shown in Figure 8, bringing the total BSS sample to 83 stars. Although the membership probabilities are generally high, spectroscopic follow-up observations would be useful to assess potential contamination from field stars and unresolved binaries. The full list of BSS and YSS candidates is presented in Appendix B.

5.7. Mass Segregation

Mass segregation is one of the key diagnostics of the dynamical evolution of stellar clusters. It arises from two-body relaxation, through which kinetic energy is redistributed among cluster members, driving the system toward partial energy equipartition. As a result, more massive stars progressively lose kinetic energy and migrate toward the cluster center, while lower-mass stars gain kinetic energy and are displaced to larger radii (S. F. Portegies Zwart et al. 2010; S. Dib et al. 2018).

To investigate this effect in Berkeley 36, cluster members were divided into four mutually exclusive classes based on their position in the CMD: supergiants ($N = 10$), giants ($N = 81$), MS stars ($N = 719$), and blue straggler stars (BSS, $N = 86$), which trace different evolutionary stages and, to first order, different stellar masses. The spatial distribution of each population was examined using the radial cumulative distribution functions (RCDFs) shown in Figure 9.

The giant population shows the steepest RCDF, rising faster than the MS distribution at all radii and indicating a stronger central concentration. The supergiant population follows a broadly similar, though noisier, trend consistent with its small sample size, remaining close to or slightly above the MS curve out to intermediate radii. In contrast, the BSS population is markedly less centrally concentrated than either the MS or

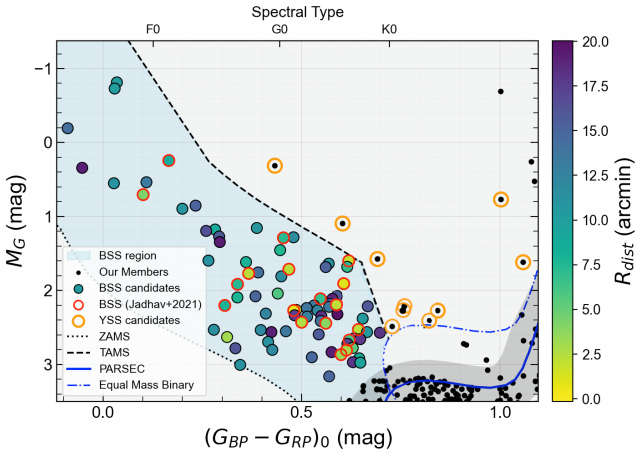


Figure 8. CMD of the Berkeley 36 in the M_G vs. $(G_{BP} - G_{RP})_0$ plane. The spectral types adopted from M. J. Pecaut & E. E. Mamajek (2013) are shown along the upper axis. The stars are color coded according to their projected distance from the cluster center, as indicated by the color scale on the right-hand side of the figure. Member stars are displayed as black dots. The solid blue line represents the best-fit PARSEC isochrone, while the dashed and dotted lines indicate the derived TAMS and the ZAMS, respectively. The blue shaded regions delineate the search areas for BSS candidates. Open orange symbols represent the identified YSS candidates, and blue inverted triangles highlight BSS following the classification by V. V. Jadhav & A. Subramaniam (2021). The gray-shaded region around the best-fit isochrone represents the uncertainty in the derived cluster age.

giant stars, with its RCDF lying below the other three curves across essentially the entire radial range.

Two-sample Kolmogorov–Smirnov (KS) tests were applied to each pair of populations to assess the statistical significance of these differences. The supergiant–MS comparison gives $p_{KS} = 0.550$, and the supergiant–giant comparison gives $p_{KS} = 0.237$, neither indicating a significant difference, consistent with the limited number of supergiants. The giant–MS comparison yields $p_{KS} = 0.071$, a marginal difference suggestive of mild central concentration among the more evolved, higher-mass stars. By contrast, the BSS population differs significantly from both the giant ($p_{KS} < 0.001$) and MS ($p_{KS} < 0.001$) distributions, confirming that its spatial distribution is statistically distinct from the rest of the cluster population.

These results indicate that the giant population is somewhat more centrally concentrated than the MS stars, consistent with expectations from mass segregation, whereas the BSS population shows the opposite behavior, being significantly more extended than both the giant and MS distributions. This is a notable departure from the classical mass-segregation picture, since BSS are typically expected to behave dynamically as relatively massive objects and to be centrally concentrated as a result of collisional or binary-mediated formation channels (e.g., C. D. Bailyn 1995; F. R. Ferraro et al. 2026). However, observations of several old OCs have shown that BSS do not always exhibit a strong central concentration and instead suggest that primordial binaries and mass-transfer processes constitute the dominant formation channel (R. D. Mathieu & A. M. Geller 2009; A. M. Geller & R. D. Mathieu 2011, 2012). In addition, numerical simulations by M. Mapelli et al. (2004, 2006) demonstrated that BSS formed through binary evolution can remain preferentially distributed in the outer regions of clusters, in contrast to collisionally formed BSS, which are expected to be more

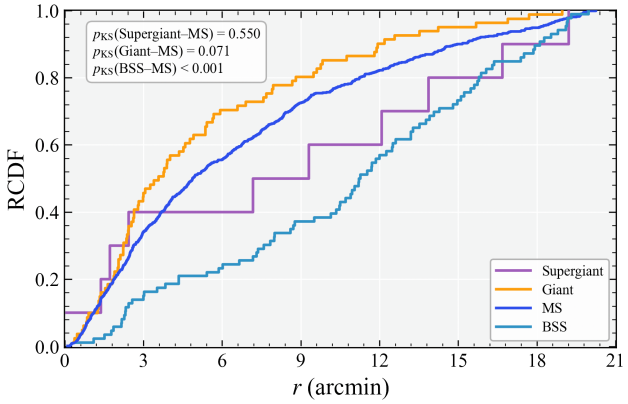


Figure 9. RCDFs of supergiant, giant, MS, and BSS populations in Berkeley 36. The radial distance corresponds to the projected angular separation from the cluster center in arcminutes. Populations were selected according to their G-band magnitude ranges and membership probabilities.

centrally concentrated. Similar conclusions have also been reached by population synthesis and Monte Carlo cluster simulations, which predict that the radial distribution of BSS is highly sensitive to the relative contributions of binary evolution and dynamical interactions (A. Hypki & M. Giersz 2017). The extended spatial distribution of BSS in Berkeley 36 is therefore consistent with these observational and theoretical studies and may instead point toward a predominantly primordial or outer-region formation origin for at least part of this population, rather than one purely governed by dynamical mass segregation.

6. Dynamical Orbital Parameters

6.1. Radial Velocity Determination

The systemic radial velocity of Berkeley 36 was derived from spectroscopic measurements in GES DR5.1 (A. Hourihane et al. 2023), as described in Section 2, and was selected over other available surveys owing to its higher spectral resolution. Following the weighting scheme of C. Soubiran et al. (2018) and R. Carrera et al. (2022), individual member velocities were combined into an inverse-variance-weighted mean, with each star assigned a weight $w_i = 1/\sigma^2_{v_{rad},i}$, from which we obtain both the cluster's systemic velocity and its internal dispersion. Based on $N = 106$ confirmed members, we derive $\langle V_{rad,OC} \rangle = 62.8 \pm 0.04$ km s^{-1} (standard error of the mean), with an internal velocity dispersion of $\sigma_{V_{rad,OC}} = 2.58$ km s^{-1}.

Figure 10 illustrates the distribution of individual stellar velocities as a function of effective temperature (T_{eff}) over the observed range (4400–5300 K). Most stars scatter tightly around the adopted mean, confirming that the sample forms a kinematically coherent group. Two stars, Gaia DR3 3032953420220233728 and Gaia DR3 3032952148909926656, lie beyond the nominal 3σ interval, yet their astrometric quality and CMD placement remain consistent with cluster membership. Their [Fe/H] values of -0.26 and -0.13 dex, respectively, are also broadly consistent with the cluster mean of -0.19 ± 0.02 dex, providing no strong evidence that they are field interlopers. We therefore interpret their discrepant velocities as the signature of orbital motion in unresolved binary systems rather than nonmembership. Excluding these two stars from the weighted mean shifts $\langle V_{rad,OC} \rangle$ by only 0.3 km s^{-1}, well within the quoted

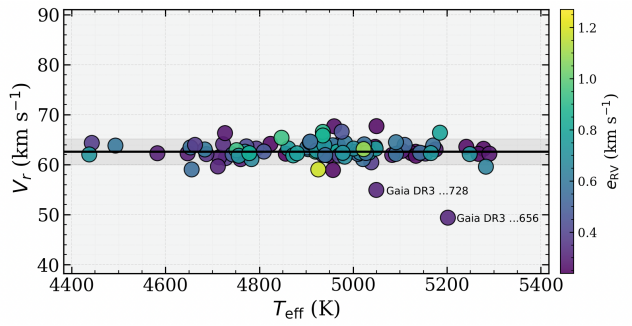


Figure 10. Radial velocity of the confirmed Berkeley 36 members plotted against effective temperature, with individual points color coded by their radial-velocity uncertainty ($e_{\rm RV}$; km s^{-1}). The horizontal solid line marks the adopted systemic velocity of the cluster, and the shaded band shows the associated 1σ dispersion about that value.

uncertainty, so their inclusion does not affect the derived systemic velocity or the kinematic conclusions drawn from it.

6.2. Cluster Orbit Analysis

To reconstruct the dynamical history of Berkeley 36, we integrated its orbit through a model Galactic potential using the `galpy` package (J. Bovy 2015). Such an analysis constrains how far the cluster has migrated radially and vertically since its formation, and how strongly it has been perturbed by the disk potential over its lifetime. Our default choice of potential is the axisymmetric MWPOTENTIAL2014, built from a Miyamoto–Nagai disk (M. Miyamoto & R. Nagai 1975), an NFW dark-matter halo (J. F. Navarro et al. 1996), and a power-law bulge with an exponential cutoff (J. Bovy & H. W. Rix 2013), so that

$$\Phi_{\rm total}(R, z) = \Phi_{\rm bulge}(r) + \Phi_{\rm disk}(R, z) + \Phi_{\rm halo}(r), \qquad (5)$$

with $r = \sqrt{R^2 + z^2}$ the spherical Galactocentric radius. As a consistency check, we repeated the integration with the MCMILLAN2017 potential (P. J. McMillan 2017), an independently calibrated mass model with updated disk and halo parameters; the two potentials produced orbital solutions that agree within their respective uncertainties. We therefore report results based on MWPOTENTIAL2014, following common practice in recent open-cluster orbit studies (e.g., T. Cantat-Gaudin et al. 2020; J. Donor et al. 2020; Y. Tarricq et al. 2021).

Because an axisymmetric potential cannot capture perturbations from the Galactic bar and spiral arms, we also tested the orbit's sensitivity to these nonaxisymmetric components. The bar was represented with `DehnenBarPotential`, i.e., a rotating quadrupolar term of the form

$$\Phi_{\rm bar}(R, \phi, t) = A(t)\cos\left[2(\phi - \Omega_{\rm bar}t)\right] f(R), \qquad (6)$$

where $\Omega_{\rm bar}$ is the pattern speed of the bar and $A(t)$ its (time-dependent) amplitude, and spiral structure was added through a steady-state spiral perturbation (`SpiralArmsPotential`). Standard literature values were adopted for the bar pattern speed ($\Omega_{\rm bar} \sim 40$ km s^{-1} kpc^{-1}), the bar scale length ($R_{\rm bar} \sim 3.5$ kpc), and a moderate perturbation amplitude, consistent with previous dynamical modeling of the Galaxy.

The six phase-space coordinates required for the integration, sky position (α, δ), heliocentric distance (d), proper motion

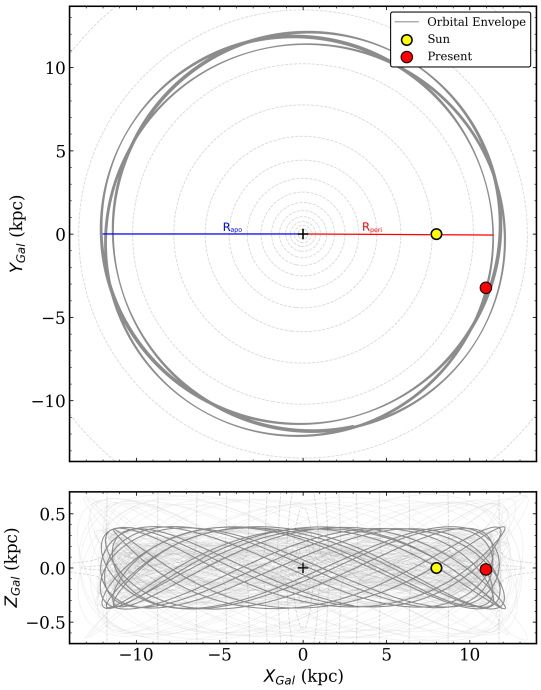


Figure 11. Reconstructed Galactic orbit of Berkeley 36. Top: projection onto the $X_{\rm Gal}$–$Y_{\rm Gal}$ plane. Bottom: projection onto the $X_{\rm Gal}$–$Z_{\rm Gal}$ plane; thin gray curves trace the family of orbits obtained from the Monte Carlo resampling of the observational uncertainties. The cluster's present-day position is marked with a filled red circle, the Sun's position with a filled yellow circle, and the background gray shading traces the Galactic mass density.

($\mu_\alpha \cos\delta$, μ_δ), and the systemic radial velocity from Section 6.1, were propagated forward and backward in time using a 1 Myr timestep, over a baseline set by the cluster's estimated age of ∼6.8 Gyr. We assumed a local circular speed of $V_{\rm rot} = 220$ km s^{-1} and a vertical solar offset of $Z_0 = 25 \pm 5$ pc (J. Bovy & S. Tremaine 2012), and converted to Galactocentric coordinates following the geometric prescription of S. Tunçel Güçtekin et al. (2019), with $R_0 = 8.2 \pm 0.1$ kpc. We also compute the cluster's guiding radius, the radius of the circular orbit that shares the cluster's specific angular momentum, as a tracer of radial mixing and possible migration (e.g., J. Binney & S. Tremaine 2008; R. Schönrich & J. Binney 2009).

To propagate observational errors into the orbital solution, we generated an ensemble of Monte Carlo realizations of the input phase-space vector and reintegrated the orbit for each realization. From the resulting distribution we derive the perigalactic distance ($R_{\rm peri}$), apogalactic distance ($R_{\rm apo}$), mean orbital radius ($R_{\rm m}$), orbital eccentricity (e), maximum vertical excursion ($Z_{\rm max}$), guiding radius ($R_{\rm g}$), and orbital period, listed in Table 1. Berkeley 36 is found to follow a nearly circular orbit, with $e = 0.036$, $R_{\rm peri} = 11.369$ kpc, and $R_{\rm apo} = 12.214$ kpc (Figure 11), giving a mean orbital radius of $R_{\rm m} \simeq 11.79$ kpc and a guiding radius of $R_{\rm g} = 11.751$ kpc—both well beyond the solar circle, placing the cluster firmly in the outer Galactic disk. The current Galactocentric distance is $R_{\rm GC} = 11.422$ kpc, closely matching $R_{\rm m}$ and $R_{\rm g}$, suggesting that the cluster is currently near its time-averaged orbital radius rather than caught in transit between extremes. The modest vertical amplitude, $Z_{\rm max} = 380$ pc, together with the low eccentricity, points to dynamically quiet, disk-like kinematics rather than a history of strong scattering. Given its outer-disk location and near-circular

motion, Berkeley 36 appears to have experienced comparatively little radial migration relative to more eccentric OCs, though we caution that any inference about its birth radius from long-term backward integration remains subject to the adopted Galactic potential and to the (still uncertain) treatment of bar and spiral perturbations, and should be read as indicative rather than definitive.

The Galactic space velocity components (U, V, W) of Berkeley 36 were computed using the GALPY package, based on the cluster's mean proper motion, distance, and radial velocity. These raw velocities were then corrected to the local standard of rest (LSR) using the solar motion values of B. Coşkunoğlu et al. (2011), namely $(U_\odot, V_\odot, W_\odot) = (8.83 \pm 0.24, 14.19 \pm 0.34, 6.57 \pm 0.21)$ km s^{-1}. This correction was applied by adding the solar motion components to the original velocities, yielding the LSR-corrected values, which are also listed in Table 1. Finally, the total space velocity of the cluster was calculated from the LSR-corrected components as

$$S_{\rm LSR} = \sqrt{U_{\rm LSR}^2 + V_{\rm LSR}^2 + W_{\rm LSR}^2}, \quad (7)$$

with the associated uncertainty obtained through standard error propagation. The resulting space velocity of Berkeley 36 is $S_{\rm LSR} = 61.36 \pm 5.48$ km s^{-1}. The obtained value falls within the velocity range typical of young thin-disk stars (S. K. Leggett 1992; P. E. Nissen 2004).

6.3. Galactic Warp and Flare Corrections

Berkeley 36 lies at a present-day Galactocentric distance of $R_{\rm GC} = 11.422$ kpc, beyond the solar circle, where both the Galactic warp and the flare of the thin disk become significant. The vertical displacement produced by the warp is modeled as

$$Z_{\rm warp}(R, \phi) = \gamma_{\rm w} [R - R_{\rm warp}] \sin(\phi - \phi_{\rm w}), \quad (8)$$

with a warp onset radius $R_{\rm warp} = 8.4$ kpc and line-of-nodes angle $\phi_{\rm w} = 5^\circ$ (S. Derriere & A. C. Robin 2001), consistent with BesanÇon-type Galaxy models (A. C. Robin et al. 2012) and 2MASS/Gaia-based studies placing the warp onset near 8–9 kpc (M. López-Corredoira et al. 2002; C. Reylé et al. 2009; Ž. Chrobáková et al. 2022). The amplitude $\gamma_{\rm w} = 0.09$ kpc^{-1} was chosen to match literature vertical displacements at $R_{\rm GC} \approx 9$–12 kpc. Orbits were then corrected via $Z_{\rm cor} = Z - Z_{\rm warp}(R, \phi)$.

The disk flare is described by a radius-dependent scale height,

$$h_z(R) = h_{z,0}[1 + \gamma_{\rm f}(R - R_0)], \quad (9)$$

with $h_{z,0} = 300$ pc and $\gamma_{\rm f} = 0.05$ kpc^{-1}, following 2MASS, SDSS, and Gaia-based measurements of outer-disk thickening (S. Bilir et al. 2006b, 2008; Y. Momany et al. 2006; A. Cabrera-Lavers et al. 2007; M. López-Corredoira & J. Molgó 2014).

Integrating the orbit in the `MWPotential2014` potential gives a maximum vertical amplitude of $Z_{\rm max} = 381$ pc, a low eccentricity of $e = 0.036$, and a mean Galactocentric radius of $R_{\rm m} = 11.79$ kpc. Once the warp correction is applied, the vertical amplitude rises to $Z_{\rm max,wf} = 709$ pc, an 86% increase, showing that the warp substantially modulates the cluster's vertical excursion at this large Galactocentric distance. The cluster remains within 100 pc of the local warp surface for only 25% of its orbital period ($W_{\rm mf}$), and the median $|Z|/h_z$ along the orbit is 0.75, compared with just 0.04 at its present-day position, indicating that Berkeley 36 currently sits close to the flared local disk plane despite reaching much greater heights elsewhere in its orbit. At its current position, the effective scale height is $h_z = 351$ pc, 17% larger than the local value, consistent with the expected outward thickening of the outer thin disk.

7. Variability Search in the Berkeley 36 Field

We inspected the available TESS observations of the high-probability members of Berkeley 36 to search for photometric variability. TESS light curves were available for eight probable cluster members. However, all of these stars exhibit very high contamination fractions (∼0.89–0.97), indicating severe source blending caused by the large TESS pixel scale in the crowded cluster field. Consequently, the extracted light curves are not suitable for reliable variability analysis, and no robust periodic variability could be established. We therefore do not identify any confirmed variable members of Berkeley 36 from the currently available TESS observations.

During the inspection of the surrounding TESS field, we identified two stars displaying well-defined eclipsing variability, namely TIC 295818770 and TIC 295818809 (Figure 12). Cross-matching with our Gaia DR3 membership catalog shows that both objects have negligible membership probabilities and are therefore unrelated foreground field stars. Both sources are also classified as detached eclipsing binaries (EA type) in the Gaia DR3 variability catalog, confirming their eclipsing nature.

The orbital periods derived from the Lomb–Scargle periodogram are $P = 3.3800 \pm 0.08$ d for TIC 295818770 and $P = 3.3902 \pm 0.07$ d for TIC 295818809. Their phased light curves exhibit deep primary eclipses and shallower secondary eclipses, characteristic of detached Algol-type eclipsing binary systems. To estimate their basic stellar parameters, we modeled their spectral energy distributions using the available multiband photometry. The resulting effective temperatures are approximately 6846 K and 7594 K for TIC 295818770 and TIC 295818809, respectively, consistent with late-F and early-A type stars. The derived distances are approximately 1.74 kpc for both systems, significantly smaller than the distance of Berkeley 36. Together with their Gaia astrometry and low membership probabilities, these results confirm that both eclipsing binaries are foreground field stars projected toward the cluster.

8. Discussion

8.1. Comparison with Previous Studies

Table 2 shows the parameter estimates that have been published for Berkeley 36 over the past decade and a half, split into a pre-Gaia group and a post-Gaia group using 2018 as the dividing line. As with most OCs in this part of the disk, the early determinations are noticeably scattered, especially for distance and age, since they relied on ground-based photometry and proper motions of limited precision. Once Gaia astrometry became available, the reported distances tightened considerably, clustering mostly between about 4 and 5 kpc, and the extinction values settled into a narrower band around $A_{\rm V} \sim 1.4$–2.0 mag.

Our own results place the cluster at $\langle d_{\rm geo} \rangle = 4377 \pm 510$ pc with $\langle A_V \rangle = 1.594 \pm 0.283$ mag, both of which sit comfortably inside the range defined by the post-Gaia literature. The metallicity we derive, [Fe/H] $= -0.19 \pm 0.02$ dex, is likewise close to the handful of spectroscopic estimates available (e.g.,

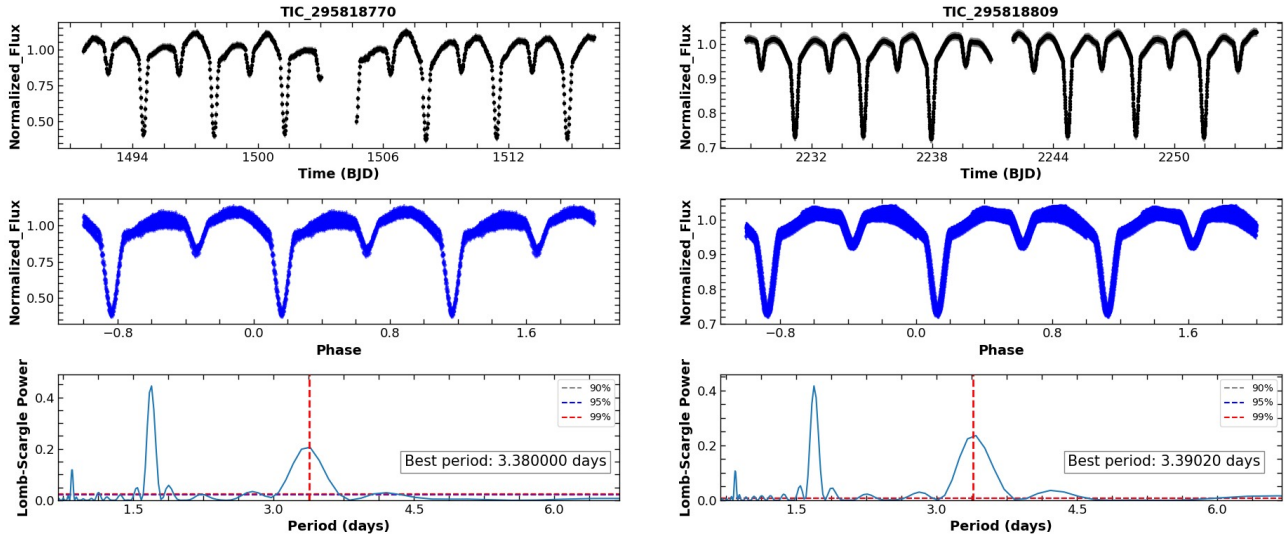


Figure 12. TESS light curves of the two foreground eclipsing binaries identified in the field of Berkeley 36. For each source, the upper panel shows the detrended TESS light curve, the middle panel presents the phase-folded light curve using the derived orbital period, and the lower panel displays the corresponding Lomb–Scargle periodogram. The adopted orbital periods are 3.3800 d for TIC 295818770 and 3.3902 d for TIC 295818809. The morphology of the phased light curves is characteristic of detached Algol-type (EA) eclipsing binaries. Both systems are foreground field stars.

Table 2
Published Astrophysical Parameters for Berkeley 36

Year	d (kpc)	A_V (mag)	Age (Myr)	[Fe/H] (dex)	References
2026	4.38	1.59	6800	−0.19	[01]
2026	⋯	⋯	6761	−0.16	[02]
2024	3.56	1.63	1820	−0.03	[03]
2023	3.88	1.95	1042	⋯	[04]
2023	4.57	1.99	4467	−0.32	[05]
2022	⋯	⋯	⋯	−0.26	[06]
2021	4.98	1.80	3412	−0.03	[07]
2020	4.37	1.42	6761	⋯	[08]
2020	4.09	1.87	1175	⋯	[09]
2014	6.14	1.26	3162	⋯	[10]
2013	5.04	1.84	2512	⋯	[11]
2011	7.54	1.42	2239	⋯	[12]

References. The horizontal line separates pre-Gaia studies; dashes indicate unreported parameters. [01] This study, [02] J. M. Otto et al. (2026), [03] L. Cavallo et al. (2024), [04] E. L. Hunt & S. Reffert (2024), [05] M. S. Angelo et al. (2023), [06] L. Spina et al. (2022), [07] W. S. Dias et al. (2021), [08] T. Cantat-Gaudin et al. (2020), [09] M. Kounkel et al. (2020), [10] W. S. Dias et al. (2014), [11] N. V. Kharchenko et al. (2013), [12] Ł. Bukowiecki et al. (2011).

W. S. Dias et al. 2021; L. Spina et al. 2022), which cluster between −0.03 and −0.32 dex. The age we obtain from isochrone fitting, 6.8 ± 0.5 Gyr, is however substantially older than most of the values quoted in the table, which mostly fall in the 1–4.5 Gyr range; only J. M. Otto et al. (2026) and T. Cantat-Gaudin et al. (2020) report ages approaching 6.8 Gyr. This discrepancy is discussed further in Section 5, where we examine how membership selection and isochrone set choice affect the derived age.

As an independent check on the isochrone age of Berkeley 36, we derived stellar ages from the age–chemical-clock relations of C. Viscasillas Vázquez et al. (2022), who calibrated multivariate relations of the form $[s/\alpha] = m_1 \cdot \mathrm{Age} + m_2 \cdot R_{\mathrm{GC}} + m_3 \cdot [\mathrm{Fe/H}] + c$ using 62 OCs observed by the Gaia-ESO survey. Since Berkeley 36 lies at $R_{\mathrm{GC}} = 11.422$ kpc, well within the outer-disk regime ($R_{\mathrm{GC}} > 9$ kpc), we adopted the outer-disk coefficients from their Table A.3, inverted to express age directly as a function of the abundance ratio, R_{rmGC}, and [Fe/H]:3, inverted to express age directly as a function of the abundance ratio, R_{GC}, and [Fe/H]:

$$\mathrm{Age} = c' + m_1' \, [s/\alpha] + m_2' \, R_{\mathrm{GC}} + m_3' \, [\mathrm{Fe/H}]. \quad (10)$$

We applied this relation to the four barium-based clocks available in our sample, [Ba/Al], [Ba/Mg], [Ba/Si], and [Ba/Ca], since ratios involving Ba show the tightest correlation with age among the indicators tested by C. Viscasillas Vázquez et al. (2022). The exclusion of [S/Fe] from the α-element abundance discussion does not affect the chemical-clock analysis, since none of the four adopted barium-based clocks ([Ba/Al], [Ba/Mg], [Ba/Si], and [Ba/Ca]) involves sulfur. Therefore, the same 10 stars and the same abundance ratios were used to derive the chemical-clock age.

Before computing ages, the individual stellar abundances were processed using the same normalization scheme as in C. Viscasillas Vázquez et al. (2022). Elemental abundances with a reported error $\geqslant$0.1 dex were discarded to avoid propagating low-quality measurements into the age relations. Each star was then classified as a giant ($\log g \leqslant 3.5$) or a dwarf ($\log g > 3.5$), and the raw [X/H] abundances were placed on a common solar scale by subtracting the corresponding M67 giant or dwarf reference abundances (Table 1 of C. Viscasillas Vázquez et al. 2022), which removes the small but nonnegligible offset between dwarf and giant abundance scales noted by the authors. Finally, for each element, the normalized abundances across the sample were cleaned using the interquartile range (IQR) criterion, rejecting values outside $[Q_1 - 1.5\,\mathrm{IQR},\ Q_3 + 1.5\,\mathrm{IQR}]$, consistent with the outlier-rejection procedure used to build the original calibration sample.

Ages were computed on a star-by-star basis for the 10 Berkeley 36 member stars with usable Ba and α-element abundances, yielding up to four individual age estimates per

star. The individual chemical clocks based on the [Ba/Al], [Ba/Mg], [Ba/Si], and [Ba/Ca] abundance ratios yield mean ages of 7.52 ± 1.54, 6.17 ± 0.76, 8.28 ± 2.08, and 5.72 ± 1.62 Gyr, respectively, demonstrating an overall consistency among the independent calibrations despite the different sample sizes available for each clock. For each star, we adopted the mean of the available clock ages and its standard deviation as an internal precision estimate. The final cluster age was then derived by averaging these star-by-star mean ages, rather than by averaging the mean ages of the individual chemical clocks. Averaging over all stars in the sample, we obtain a mean cluster age of $\langle t \rangle \simeq 7.75 \pm 1.94$ Gyr, in reasonable agreement with the isochrone age of 6.8 ± 0.5 Gyr. The relatively large star-to-star scatter is not unexpected: C. Viscasillas Vázquez et al. (2022) report a precision of about 0.9 Gyr for the [Ba/Al] relation in the outer disk when applied to cluster-averaged abundances, but individual member stars in their own sample show appreciably larger dispersion (their Figure 9), reflecting both measurement uncertainties in the neutron-capture-element abundances and the intrinsic nonuniqueness of any single age–chemical-clock relation (see their Section 7). Given that Berkeley 36 is located in the outer disk, where radial migration is expected to play a comparatively minor role (C. Viscasillas Vázquez et al. 2022), we consider the chemical-clock age estimate to be a genuine, largely unbiased confirmation of the isochrone-based age, rather than an estimate confused by migrated interlopers.

8.2. Chemical Birth Radius and Radial Migration

The chemical birth radius (R_b) of Berkeley 36 was estimated following the chemo-dynamical approach of I. Minchev et al. (2018), as adopted in subsequent studies (e.g., Y. L. Lu et al. 2024; B. Ratcliffe et al. 2025, 2026; D. C. Çınar et al. 2026b). In this context, R_b is inferred from the cluster's age and metallicity under the assumption of a time-dependent Galactic radial metallicity gradient. Using $[Fe/H] = -0.19 \pm 0.02$ dex and an age of ≈6.8 ± 0.5 Gyr, we obtain $R_b = 6.71 \pm 0.66$ kpc, smaller than the solar radius ($R_\odot \approx 8.2$ kpc), suggesting an inner-disk origin. This estimate depends on the adopted chemo-dynamical model and should be regarded as approximate rather than a unique solution.

Comparing R_b with the cluster's present-day guiding radius ($R_g = 11.751$ kpc) and Galactocentric radius ($R_{GC} = 11.422$ kpc) yields $|R_g - R_b| = 5.04$ kpc and $|R_{GC} - R_b| = 4.71$ kpc, while the offset between R_g and R_{GC} itself is only $|R_g - R_{GC}| = 0.33$ kpc. Following the usual interpretation, the difference between the guiding radius and the birth radius, $R_g - R_b$, is commonly interpreted as an estimate of the cumulative effect of churning, i.e., the long-term change in guiding-center radius driven by angular-momentum exchange with spiral arms and the Galactic bar (J. A. Sellwood & J. J. Binney 2002; F. Anders et al. 2017). Recent cosmological simulations show that spiral-arm interactions can drive significant outward migration of open clusters through churning without substantial kinematic heating (A. I. Wiggins et al. 2025). In contrast, the difference between the present-day Galactocentric radius and the birth radius, $R_{GC} - R_b$, reflects the combined effects of churning and epicyclic motion (blurring), whereas the offset $R_{GC} - R_g$ represents the contribution from epicyclic motion alone, arising from orbital eccentricity (J. Binney & S. Tremaine 2008; J. A. Sellwood & J. J. Binney 2002). For Berkeley 36, the blurring contribution is small, consistent with its low orbital eccentricity ($e = 0.036$). Therefore, the inferred radial migration is expected to be dominated by churning, with only a minor contribution from epicyclic blurring. Since $R_g > R_b$, Berkeley 36 has migrated outward from an inner-disk birth site to its current position well beyond the solar circle.

Figure 13 places Berkeley 36 in the age–radius-deviation plane together with the OC sample of J. M. Otto et al. (2026). At an age of ∼6.8 Gyr, the cluster's $|R_g - R_b| = 5.04$ kpc (panel (a)) and $|R_{GC} - R_b| = 4.71$ kpc (panel (b)) lie clearly above the empirical secular-heating envelopes of N. Frankel et al. (2018) and N. Frankel et al. (2020), which reach only ∼3 kpc by this age. This places Berkeley 36 among the small number of old clusters in the comparison sample with the largest inferred migration distances, alongside a handful of J. M. Otto et al. (2026) clusters at similar ages (∼7–7.3 Gyr) showing comparably large offsets (∼5.2–5.3 kpc). Berkeley 36 is therefore not an isolated outlier but part of a small population of old OCs whose inferred radial migration exceeds that expected from standard secular evolution involving both churning and blurring, suggesting that stronger or more episodic angular-momentum exchange, for example, transient spiral structure or bar-resonance scattering, may have acted on this cluster's orbit, in addition to or instead of steady-state secular diffusion. As with the extreme values seen among the youngest clusters in the sample ($t < 0.5$ Gyr, $|R_g - R_b|$ up to ∼6.5 kpc), part of the offset could also reflect uncertainties in the adopted birth-radius model, the metallicity gradient, or the orbital parameters, and this caveat should be kept in mind when interpreting Berkeley 36's position above the envelope.

Normalizing the migration distance by age gives an effective rate of $|R_g - R_b|/t \approx 0.74$ kpc Gyr^{-1} (and ≈0.69 kpc Gyr^{-1} using R_{GC} instead of R_g), somewhat below the 1.0 ± 0.6 kpc Gyr^{-1} inferred here for the older J. M. Otto et al. (2026) clusters with $|\Delta R| > 1$ kpc, and below the 1.5 ± 0.5 kpc Gyr^{-1} reported by Y. Q. Chen & G. Zhao (2020). This indicates that, while individually large, Berkeley 36's total migration distance is still broadly consistent with several gigayears of sustained radial mixing, rather than requiring an implausibly fast migration episode, even though its position above the Frankel envelopes suggests it has migrated further than the population's typical secular-heating expectation for its age.

Berkeley 36's inner-disk birth radius ($R_b = 6.71$ kpc) combined with its mildly subsolar metallicity ([Fe/H] = −0.19 dex) is broadly consistent with the negative radial metallicity gradient expected from inside-out disk formation (e.g., C. Chiappini et al. 1997; I. Minchev et al. 2014), although its metallicity is only moderately depleted relative to solar for its inferred birth radius, which may reflect intrinsic scatter in the adopted gradient or the cluster's subsequent migration history. Taken together, the large outward displacement from R_b to R_{GC}, the dominance of churning over blurring, and the cluster's old age (∼6.8 Gyr) support a scenario in which Berkeley 36 may have formed in the inner disk and subsequently migrated outward through secular radial migration, making it a useful benchmark for probing strong-migration outliers relative to the general old-cluster population.

9. Summary and Conclusion

In this study, we have presented a comprehensive, multi-wavelength characterization of the OC cluster Berkeley 36, combining Gaia DR3 astrometry and photometry with high-resolution spectroscopy from GES DR5.1 in a single, internally consistent analysis. By anchoring the cluster's

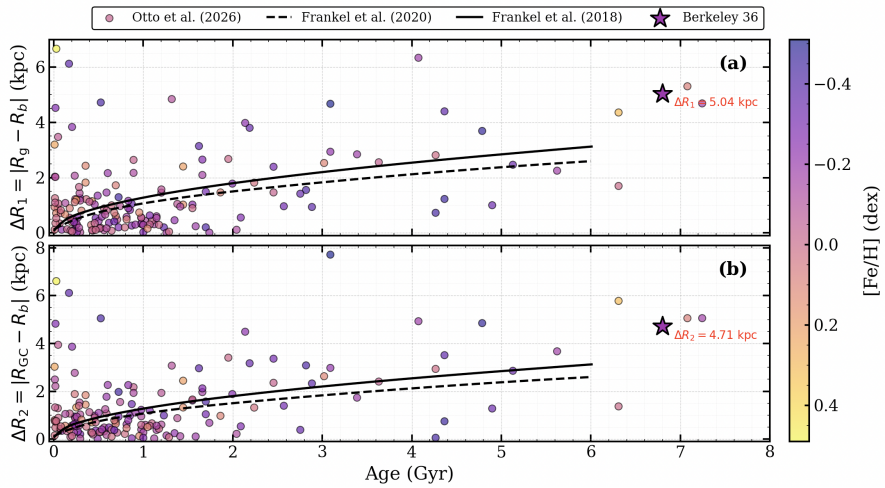


Figure 13. Distribution of OCs in the $|R_g - R_b| \times t$ (panel (a)) and $|R_{GC} - R_b| \times t$ (panel (b)) planes. Colors indicate the cluster metallicity ([Fe/H]). The circular symbols correspond to the OC sample of J. M. Otto et al. (2026), while Berkeley 36 is marked with a star symbol. The solid and dashed black curves show the empirical age-dependent limits reported by N. Frankel et al. (2018) and N. Frankel et al. (2020), respectively.

metallicity and distance with independent astrometric and spectroscopic constraints, we reduced the classical age–reddening–metallicity degeneracy to a single free parameter, allowing us to derive a self-consistent set of structural, chemical, kinematic, and dynamical properties for Berkeley 36. Our principal results can be summarized as follows:

1. Using a GMM applied to Gaia DR3 proper motions and parallaxes, we identified $N_{\rm mem} = 946$ probable members of Berkeley 36 at $P \geqslant 0.7$, centered at $\alpha = 07^{\rm h}16^{\rm m}23^{\rm s}.86$, $\delta = -13^{\circ}11'51''.35$, with a mean proper motion of $(-1.701 \pm 0.163, 0.960 \pm 0.154)$ mas yr^{-1} and a parallax-based distance of $d_{\varpi} = 4.46 \pm 2.43$ kpc.
2. The radial density profile, fitted with a I. King (1962) model via MCMC, yields a core radius $r_c = 2.63^{+0.22}_{-0.21}$ arcmin and a tidal radius $r_t = 14.84^{+0.47}_{-0.47}$ arcmin, corresponding to a concentration parameter $C \approx 0.75$, characteristic of a moderately concentrated, dynamically relaxed system.
3. Fixing the metallicity from GES spectroscopy ($\langle$[Fe/H]$\rangle = -0.19 \pm 0.02$ dex) and the distance and reddening from photometric/astrometric data ($\langle d \rangle = 4377 \pm 510$ pc, $\langle A_G \rangle = 1.350 \pm 0.045$ mag), isochrone fitting with both PARSEC and MIST models gives a consistent cluster age of 6.8 ± 0.5 Gyr.
4. Independent Ba-based chemical clocks, combining the [Ba/Al], [Ba/Mg], [Ba/Si], and [Ba/Ca] abundance ratios, yield a mean cluster age of $\langle t \rangle \simeq 7.75 \pm 1.94$ Gyr from star-by-star estimates, in good agreement with the isochrone age of 6.8 ± 0.5 Gyr.
5. A photometric analysis of the main sequence reveals a binary fraction of $f_b = 0.480 \pm 0.017$, with the mass-ratio distribution peaking at $q \sim 0.8$–0.9, mirroring the pattern previously found for Berkeley 32.
6. We identified 83 BSS candidates (18 previously known and 65 newly detected) and 10 YSS candidates. Unexpectedly, the BSS population is significantly less centrally concentrated than the giant and main-sequence populations, in contrast to the classical mass-segregation picture, suggesting a substantial primordial or outer-region contribution to this population.
7. The cluster's systemic radial velocity, derived from $N = 106$ GES members, is $\langle V_{\rm rad,OC} \rangle = 62.80 \pm 0.04$ km s^{-1}, with an internal dispersion of $\sigma_{V_{\rm rad,OC}} = 2.58$ km s^{-1}, confirming that the sample forms a kinematically coherent group.
8. Orbit integration in the MWPOTENTIAL2014 potential shows that Berkeley 36 follows a nearly circular orbit ($e = 0.036 \pm 0.027$) in the outer disk, with a guiding radius $R_g = 11.751 \pm 0.772$ kpc and a current Galactocentric distance $R_{GC} = 11.422 \pm 0.437$ kpc. Accounting for the Galactic warp increases the maximum vertical excursion by 86%, while the Galactic disk flare increases the local scale height by 17%, highlighting the importance of both effects at large Galactocentric radii.
9. The chemical birth radius, $R_b = 6.71 \pm 0.66$ kpc, lies well inside the cluster's present-day guiding radius, implying an outward migration of $\sim$5 kpc dominated by churning rather than blurring. This places Berkeley 36 among the old OCs with the largest inferred migration distances relative to its age, exceeding the secular-heating expectations of N. Frankel et al. (2018) and N. Frankel et al. (2020).
10. A search for photometric variability in the TESS field of Berkeley 36 did not yield any confirmed cluster-member variables, owing to severe blending in the crowded field; the two eclipsing binaries detected nearby (TIC 295818770 and TIC 295818809) were found to be unrelated foreground field stars.

These results depict Berkeley 36 as an old, dynamically evolved OC that may have formed in the inner Galactic disk and subsequently migrated outward to its present location beyond the solar circle, primarily through churning rather than orbital blurring. Its large migration distance relative to its age, together with its centrally concentrated giant population and unusually extended BSS distribution, makes Berkeley 36 a valuable benchmark for studies of secular disk evolution and cluster dynamical history. Further progress on this system would benefit from spectroscopic follow-up of the BSS candidates to assess field contamination and binarity, deeper or higher-cadence photometric monitoring capable of overcoming the blending limitations of TESS in this crowded field, and the inclusion of Berkeley 36 in future homogeneous, Galaxy-wide compilations of migration histories as additional spectroscopic and astrometric data become available.

Acknowledgments

We sincerely thank the referee and the data editor for their constructive comments and valuable suggestions, which have helped us improve the quality, clarity, and overall presentation of this manuscript. I.-G.J. acknowledges support from the National Science and Technology Council (NSTC), Taiwan, under grants NSTC 113-2112-M-007-030 and NSTC 114-2112-M-007-029. This study is a part of the PhD Thesis of Deniz Cennet Çinar. This work uses data from the European Space Agency's Gaia mission, processed by the Gaia Data Processing and Analysis Consortium (DPAC). Based on data obtained from the ESO Science Archive Facility with DOI: 10.18727/archive/25.

Facilities: Gaia, PS1, TESS, CTIO:2MASS.

Software: `astropy` (Astropy Collaboration et al. 2013, 2018; Astropy Collaboration et al. 2022), `Matplotlib` (J. D. Hunter 2007), `NumPy` (C. R. Harris et al. 2020), `SciPy` (P. Virtanen et al. 2020), `scikit-learn` (F. Pedregosa et al. 2011), `emcee` (D. Foreman-Mackey et al. 2013), `galpy` (J. Bovy 2015).

Appendix A
Gaia DR3 Data Retrieval and Quality Filtering

Table A1 summarizes the photometric precision of the Gaia DR3 catalog compiled for Berkeley 36 after the quality-selection steps described below. Sources were queried from the Gaia DR3 archive through an ADQL statement centered on the cluster coordinates, adopting a search radius of 21′ and restricting the query to sources brighter than $G = 21$ mag. For clarity, only the core selection conditions (sky position, search cone, and magnitude limit) are given in the main text; the complete ADQL statement is not reproduced here for brevity.

Prior to the membership computation, we required all retrieved sources to have a full five-parameter astrometric solution, as identified by the `astrometric_params_solved` flag. This step guarantees that proper motions and parallaxes are simultaneously available for every star entering the subsequent membership determination. Sources flagged as having a less robust astrometric solution were not discarded outright; instead, they were kept in the working catalog, since their effect on the final membership probabilities is expected to be minor—stars with poorly constrained astrometry tend to scatter away from the cluster locus in proper-motion/parallax space and are consequently assigned low membership probabilities by construction. Applying these criteria to the initial query results in a working sample of 27,016 sources in the direction of Berkeley 36, as listed in Table A1.

Table A1
Mean Photometric Uncertainties in Gaia G Magnitude and ($G_{BP} - G_{RP}$) Color for Sources Toward Berkeley 36, Binned by Apparent Magnitude

G (mag)	N	σ_G	$\sigma_{G_{BP}-G_{RP}}$
6–14	406	0.003	0.006
14–15	475	0.003	0.005
15–16	894	0.003	0.006
16–17	1723	0.003	0.009
17–18	2913	0.003	0.015
18–19	4642	0.003	0.034
19–20	6533	0.004	0.070
20–21	8237	0.009	0.175
21–23	1193	0.023	0.401
Total	27016	0.006	0.097

We further examined how the photometric errors evolve with apparent magnitude before proceeding to the color–magnitude diagram analysis. As anticipated, both the G-band and ($G_{BP} - G_{RP}$) uncertainties stay small at the bright end of the sample and grow steadily toward fainter stars, with a pronounced steepening past $G \sim 20$ mag. The magnitude-binned statistics in Table A1 quantify this behavior directly. Guided by this trend, we restrict the photometric sample used for the CMD analysis to $G \leqslant 20.5$ mag, a choice that keeps the bulk of the well-measured stars while excluding the regime where color errors rise sharply and could otherwise distort the cluster sequence.

Appendix B
Blue and Yellow Straggler Star Catalog

Table B1 lists the full sample of blue straggler star (BSS) and yellow straggler star (YSS) candidates discussed in Section 5.6, together with the variable stars identified toward the cluster from the Gaia DR3 variability classification. For each object, we provide the equatorial coordinates, the G-band magnitude, the cluster membership probability, and the star type (BSS or YSS). The superscript [a] indicates the origin of the BSS/YSS identification: (1) V. V. Jadhav & A. Subramaniam (2021); (2) this work.

Table B1
Full List of BSS and YSS Candidates Identified Toward the Cluster, Together with Their Membership Probabilities

No.	α (hh:mm:ss)	δ (dd:mm:ss)	G (mag)	P	Type	References[a]	No.	α (hh:mm:ss)	δ (dd:mm:ss)	G (mag)	P	Type	References[a]
01	07:16:26.60	−13:11:42.1	16.64	1.00	BSS	1	48	07:16:39.93	−13:00:30.6	17.17	0.84	BSS	2
02	07:16:27.09	−13:11:05.5	16.28	1.00	BSS	1	49	07:16:26.63	−12:59:36.4	16.64	1.00	BSS	2
03	07:16:29.41	−13:12:32.6	16.63	0.99	BSS	2	50	07:16:35.55	−13:24:00.3	16.68	0.82	BSS	2
04	07:16:21.55	−13:10:10.5	17.32	1.00	BSS	2	51	07:15:38.38	−13:06:01.9	17.33	1.00	BSS	2
05	07:16:30.18	−13:12:53.1	15.97	1.00	BSS	1	52	07:17:15.58	−13:11:00.1	16.72	0.97	BSS	2
06	07:16:24.67	−13:14:00.1	16.88	1.00	BSS	2	53	07:17:02.91	−13:21:00.3	16.57	1.00	BSS	2
07	07:16:19.51	−13:09:57.7	16.56	0.99	BSS	1	54	07:16:58.50	−13:01:42.1	16.59	1.00	BSS	2
08	07:16:20.66	−13:09:43.3	16.90	1.00	BSS	1	55	07:16:01.01	−12:59:47.6	14.90	1.00	BSS	2
09	07:16:24.46	−13:09:32.8	16.14	1.00	BSS	1	56	07:17:10.15	−13:19:20.8	16.92	1.00	BSS	2
10	07:16:24.33	−13:14:10.8	16.08	1.00	BSS	1	57	07:17:01.40	−13:01:33.4	16.60	1.00	BSS	2
11	07:16:25.10	−13:09:26.1	17.09	0.99	BSS	2	58	07:17:16.40	−13:06:22.6	16.78	0.97	BSS	2
12	07:16:34.03	−13:11:09.7	16.80	1.00	BSS	1	59	07:16:47.94	−12:59:03.4	16.12	0.72	BSS	2
13	07:16:25.14	−13:08:52.8	17.17	1.00	BSS	1	60	07:15:59.00	−13:24:47.8	14.17	1.00	BSS	2
14	07:16:34.87	−13:10:27.0	17.00	0.70	BSS	2	61	07:15:57.16	−13:25:09.6	17.27	0.86	BSS	2
15	07:16:20.18	−13:15:15.7	17.23	1.00	BSS	1	62	07:17:08.97	−13:01:41.3	16.45	1.00	BSS	2
16	07:16:11.19	−13:09:34.9	16.81	1.00	BSS	1	63	07:15:26.78	−13:05:56.7	15.22	0.80	BSS	2
17	07:16:40.00	−13:10:00.1	15.07	0.76	BSS	1	64	07:15:59.57	−12:57:48.8	16.05	1.00	BSS	2
18	07:16:03.66	−13:14:08.5	17.14	0.88	BSS	2	65	07:15:49.75	−12:58:47.5	15.64	0.89	BSS	2
19	07:16:04.21	−13:08:26.8	16.41	0.98	BSS	2	66	07:17:08.68	−13:00:41.7	16.96	1.00	BSS	2
20	07:16:16.00	−13:06:08.7	17.04	1.00	BSS	1	67	07:15:55.21	−12:57:44.9	17.01	1.00	BSS	2
21	07:16:34.06	−13:18:01.7	16.48	0.81	BSS	1	68	07:15:19.75	−13:09:26.9	16.58	0.95	BSS	2
22	07:16:21.64	−13:04:42.0	16.05	1.00	BSS	2	69	07:17:28.68	−13:10:06.3	16.55	1.00	BSS	2
23	07:16:40.10	−13:18:00.6	15.66	0.86	BSS	1	70	07:17:28.58	−13:15:04.4	17.15	0.71	BSS	2
24	07:16:32.53	−13:18:55.1	16.28	1.00	BSS	1	71	07:16:23.16	−12:55:28.8	15.56	0.89	BSS	2
25	07:16:22.74	−13:19:26.7	15.82	0.95	BSS	2	72	07:16:38.46	−13:28:52.8	17.09	1.00	BSS	2
26	07:16:49.99	−13:07:16.9	16.46	0.94	BSS	2	73	07:17:23.79	−13:21:33.9	16.70	1.00	BSS	2
27	07:16:23.10	−13:19:50.6	16.57	0.99	BSS	1	74	07:15:10.50	−13:12:30.6	17.34	1.00	BSS	2
28	07:16:53.52	−13:15:19.2	15.98	0.98	BSS	2	75	07:17:21.41	−13:00:40.2	17.03	1.00	BSS	2
29	07:16:58.53	−13:13:30.3	17.29	0.89	BSS	2	76	07:15:16.41	−13:19:32.0	16.94	0.98	BSS	2
30	07:15:48.27	−13:12:48.4	15.54	1.00	BSS	2	77	07:15:34.13	−13:25:33.6	16.71	0.99	BSS	2
31	07:16:59.77	−13:12:31.6	14.61	0.99	BSS	1	78	07:17:33.39	−13:03:41.1	16.48	0.96	BSS	2
32	07:17:02.46	−13:13:23.1	17.34	0.93	BSS	2	79	07:17:23.84	−12:59:32.0	17.20	1.00	BSS	2
33	07:17:03.09	−13:15:17.6	13.64	0.80	BSS	2	80	07:15:10.13	−13:05:12.4	16.93	0.95	BSS	2
34	07:17:05.28	−13:14:11.6	13.55	1.00	BSS	2	81	07:15:37.11	−13:27:17.6	14.71	0.97	BSS	2
35	07:15:58.01	−13:20:13.8	16.75	0.98	BSS	2	82	07:16:46.23	−12:53:19.3	15.71	1.00	BSS	2
36	07:15:56.25	−13:03:47.6	16.93	1.00	BSS	2	83	07:17:28.68	−12:59:37.6	16.69	1.00	BSS	2
37	07:16:31.22	−13:22:25.2	15.52	0.92	BSS	2	84	07:16:23.43	−13:15:58.2	15.99	1.00	YSS	2
38	07:17:06.35	−13:15:17.2	16.00	0.99	BSS	2	85	07:16:41.65	−13:12:05.5	16.61	1.00	YSS	2
39	07:17:06.53	−13:08:21.7	15.26	0.98	BSS	2	86	07:16:40.28	−13:20:19.8	16.64	1.00	YSS	2
40	07:16:13.07	−13:22:35.8	14.92	0.72	BSS	2	87	07:15:46.08	−13:04:03.2	15.94	1.00	YSS	2
41	07:17:09.81	−13:11:07.8	15.96	1.00	BSS	2	88	07:16:01.98	−13:00:23.1	15.14	0.82	YSS	2
42	07:15:53.01	−13:03:31.1	17.37	0.89	BSS	2	89	07:17:20.06	−13:07:25.5	15.46	1.00	YSS	2
43	07:17:09.66	−13:13:30.2	17.06	0.97	BSS	2	90	07:16:58.68	−13:24:34.0	14.68	0.89	YSS	2
44	07:16:49.79	−13:21:31.1	16.90	0.77	BSS	2	91	07:15:22.90	−13:18:37.8	16.45	0.98	YSS	2
45	07:16:25.93	−13:00:09.9	16.18	1.00	BSS	2	92	07:17:15.66	−12:59:25.5	16.78	1.00	YSS	2
46	07:17:05.02	−13:17:54.9	15.65	1.00	BSS	2	93	07:15:08.05	−13:10:01.4	16.64	1.00	YSS	2
47	07:16:20.69	−13:00:01.3	16.90	1.00	BSS	2							

Note. The superscript [a] indicates the source of the identification: (1) V. V. Jadhav & A. Subramaniam (2021); (2) this work.
(This table is available in its entirety in machine-readable form in the online article.)

ORCID iDs

Deniz Cennet Çınar https://orcid.org/0000-0001-7940-3731
D. Bisht https://orcid.org/0000-0002-8988-8434
Ing-Guey Jiang https://orcid.org/0000-0001-7359-3300
Selçuk Bilir https://orcid.org/0000-0003-3510-1509

References

Agarwal, M., Rao, K. K., Vaidya, K., & Bhattacharya, S. 2021, MNRAS, 502, 2582
Ak, T., Bostancı, Z. F., Yontan, T., et al. 2016, Ap&SS, 361, 126
Akbulut, B., Ak, S., Yontan, T., et al. 2021, Ap&SS, 366, 68
Allen, C., & Santillan, A. 1991, RMxAA, 22, 255
Alzhrani, A. Y., HarooN, A. A., Elsanhoury, W. H., & Çınar, D. C. 2025a, JApA, 46, 50
Alzhrani, A. Y., HarooN, A. A., Elsanhoury, W. H., & Çınar, D. C. 2025b, JApA, 46, 58
Anders, F., Chiappini, C., Rodrigues, T. S., et al. 2017, A&A, 597, A30
Andreuzzi, G., Bragaglia, A., Tosi, M., & Marconi, G. 2011, MNRAS, 412, 1265
Andronov, N., Pinsonneault, M. H., & Terndrup, D. M. 2006, ApJ, 646, 1160
Angelo, M. S., Santos, J. F. C., Jr., Maia, F. F. S., & Corradi, W. J. B. 2023, MNRAS, 522, 956
Astropy Collaboration, Price-Whelan, A. M., Lim, P. L., et al. 2022, ApJ, 935, 167
Astropy Collaboration, Price-Whelan, A. M., Sipőcz, B. M., et al. 2018, AJ, 156, 123
Astropy Collaboration, Robitaille, T. P., Tollerud, E. J., et al. 2013, A&A, 558, A33
Bailer-Jones, C. A. L., Rybizki, J., Fouesneau, M., Demleitner, M., & Andrae, R. 2021, AJ, 161, 147
Bailyn, C. D. 1995, ARA&A, 33, 133
Banks, T., Yontan, T., Bilir, S., & Canbay, R. 2020, JApA, 41, 6
Bastian, N., Kamann, S., Niederhofer, F., & Saracino, S. 2025, A&A, 700, A241
Belwal, K., Bisht, D., Jiang, I.-G., et al. 2026, AJ, 171, 288
Belwal, K., Bisht, D., Jiang, I.-G., et al. 2025, MNRAS, 544, 988
Bilir, S., Cabrera-Lavers, A., Karaali, S., et al. 2008, PASA, 25, 69
Bilir, S., Güver, T., & Aslan, M. 2006a, AN, 327, 693
Bilir, S., Güver, T., Khamitov, I., et al. 2010, Ap&SS, 326, 139
Bilir, S., Karaali, S., Güver, T., Karataş, Y., & Ak, S. G. 2006b, AN, 327, 72
Bilir, S., Karataş, Y., Demircan, O., & Eker, Z. 2005, MNRAS, 357, 497
Bilir, S., Taşdemir, S., Eraydın, E., et al. 2026, A&A, 26, 085002
Bilir, S., Bostancı, Z. F., Yontan, T., et al. 2016, AdSpR, 58, 1900
Binney, J., & Tremaine, S. 2008, Galactic Dynamics: Second Edition (Princeton Univ. Press)
Bisht, D., Jiang, I.-G., Elsanhoury, W. H., et al. 2026a, AJ, 171, 72
Bisht, D., Jiang, I.-G., Belwal, K., et al. 2026b, ApJ, 1003, 182
Bisht, D., Jiang, I.-G., Belwal, K., et al. 2026c, MNRAS,
Boch, T., Pineau, F., & Derriere, S. 2012, ASPC, 461, 291
Bossini, D., Vallenari, A., Bragaglia, A., et al. 2019, A&A, 623, A108
Bostancı, Z. F., Ak, T., Yontan, T., et al. 2015, MNRAS, 453, 1095
Bostancı, Z. F., Yontan, T., Bilir, S., et al. 2018, Ap&SS, 363, 143
Bovy, J. 2015, ApJS, 216, 29
Bovy, J. 2016, ApJ, 817, 49
Bovy, J., & Rix, H. W. 2013, ApJ, 779, 115
Bovy, J., & Tremaine, S. 2012, ApJ, 756, 89
Bragaglia, A., Fu, X., Mucciarelli, A., Andreuzzi, G., & Donati, P. 2018, A&A, 619, A176
Bragaglia, A., Sestito, P., Villanova, S., et al. 2008, A&A, 480, 79
Bressan, A., Marigo, P., Girardi, L., et al. 2012, MNRAS, 427, 127
Bukowiecki, Ł., Maciejewski, G., Konorski, P., & Strobel, A. 2011, AcA, 61, 231
Burki, G. 1975, A&A, 43, 37
Cabrera-Lavers, A., Bilir, S., Ak, S., Yaz, E., & López-Corredoira, M. 2007, A&A, 464, 565
Canbay, R., Bilir, S., Özdönmez, A., & Ak, T. 2023, AJ, 165, 163
Canbay, R., Çınar, D. C., Çalışkan, Ö., et al. 2026, arXiv:2606.31714
Cantat-Gaudin, T., Anders, F., Castro-Ginard, A., et al. 2020, A&A, 640, A1
Cantat-Gaudin, T., Jordi, C., Vallenari, A., et al. 2018, A&A, 618, A93
Cantat-Gaudin, T., Anders, F., Castro-Ginard, A., et al. 2020, A&A, 640, A1
Cardelli, J. A., Clayton, G. C., & Mathis, J. S. 1989, ApJ, 345, 245
Carraro, G., Geisler, D., Villanova, S., Frinchaboy, P. M., & Majewski, S. R. 2007, A&A, 476, 217
Carraro, G., Turner, D. G., Majaess, D. J., et al. 2017, AJ, 153, 156
Carrera, R., & Pancino, E. 2011, A&A, 535, A30
Carrera, R., Bragaglia, A., Cantat-Gaudin, T., et al. 2019, A&A, 623, A80
Carrera, R., Casamiquela, L., Carbajo-Hijarrubia, J., et al. 2022, A&A, 658, A14
Castro-Ginard, A., Jordi, C., Luri, X., et al. 2020, A&A, 635, A45
Cavallo, L., Spina, L., Carraro, G., et al. 2024, AJ, 167, 12
Çakmak, H., Yontan, T., Bilir, S., et al. 2024, AN, 345, e20240054
Çınar, D. C., Bilir, D. C., Şahin, S., & Plevne, O. 2025, AJ, 170, 13
Çınar, D. C., Bisht, D., Bilir, S., Qin, S., & Saker, L. 2026a, ApJ, 1006, 109
Çınar, D. C., Bisht, D., Jiang, I. G., et al. 2026b, AJ, 172, 140
Çınar, D. C., Elsanhoury, W. H., & Haroon, A. A. 2026c, NewA, 125, 102532
Çınar, D. C., Taşdemir, S., Koç, S., & Iyer, S. 2024, PARep, 2, 1
Chen, Y. Q., & Zhao, G. 2020, MNRAS, 495, 2673
Chiappini, C., Matteucci, F., & Gratton, R. 1997, ApJ, 477, 765
Choi, J., Dotter, A., Conroy, C., et al. 2016, ApJ, 823, 102
Chrobáková, Ž., Nagy, R., & López-Corredoira, M. 2022, A&A, 664, A58
Coşkunoğlu, B., Ak, S., Bilir, S., et al. 2011, MNRAS, 412, 1237
Cover, T., & Hart, P. 1967, ITIT, 13, 21
Demircan, O., Eker, Z., Karataş, Y., & Bilir, S. 2006, MNRAS, 366, 1511
Dempster, A. P., Laird, N. M., & Rubin, D. B. 1977, J. R. Stat. Soc., 39, 1
Derriere, S., & Robin, A. C. 2001, ASPC, 232, 229
Dias, W. S., Alessi, B. S., Moitinho, A., & Lépine, J. R. D. 2002, A&A, 389, 871
Dias, W. S., Monteiro, H., Caetano, T. C., et al. 2014, A&A, 564, A79
Dias, W. S., Monteiro, H., Moitinho, A., et al. 2021, MNRAS, 504, 356
Dib, S., Schmeja, S., & Parker, R. J. 2018, MNRAS, 473, 849
Donada, J., Anders, F., Jordi, C., et al. 2023, A&A, 675, A89
Döner, S., Ak, S., Önal taş, Ö., & Plevne, O. 2023, PARep, 1, 11
Donor, J., Frinchaboy, P. M., Cunha, K., et al. 2020, AJ, 159, 199
Dotter, A. 2016, ApJS, 222, 8
Eker, Z., Bilir, S., Soydugan, F., et al. 2014, PASA, 31, e024
Eker, Z., Demircan, O., Bilir, S., & Karataş, Y. 2006, MNRAS, 373, 1483
Eker, Z., Soydugan, F., & Bilir, S. 2024, PARep, 2, 41
Eker, Z., Soydugan, F., Soydugan, E., et al. 2015, AJ, 149, 131
Eker, Z., Bakış, V., Bilir, S., et al. 2018, MNRAS, 479, 5491
Elsanhoury, W. H., Haroon, A. A., Elkholy, E. A., & Çınar, D. C. 2025, JApA, 46, 21
Elsanhoury, W. H., Taşdemir, S., Çınar, D. C., et al. 2026, RAA, 26, 035020
Ferraro, F. R., Lanzoni, B., Vesperini, E., et al. 2026, NatCo, 17, 768
Foreman-Mackey, D., Hogg, D. W., Lang, D., & Goodman, J. 2013, PASP, 125, 306
Frankel, N., Rix, H. W., Ting, Y. S., Ness, M., & Hogg, D. W. 2018, ApJ, 865, 96
Frankel, N., Sanders, J., Ting, Y. S., & Rix, H. W. 2020, ApJ, 896, 15
Friel, E. D. 1995, ARA&A, 33, 381
Friel, E. D., Janes, K. A., Tavarez, M., et al. 2002, AJ, 124, 2693
Gaia Collaboration, Brown, A. G. A., Vallenari, A., et al. 2018, A&A, 616, A1
Gaia Collaboration, Brown, A. G. A., Vallenari, A., et al. 2021, A&A, 649, A1
Gaia Collaboration, Prusti, T., de Bruijne, J. H. J., et al. 2016, A&A, 595, A1
Gaia Collaboration, Vallenari, A., Brown, A. G. A., et al. 2023, A&A, 674, A1
Geller, A. M., & Mathieu, R. D. 2011, Natur, 478, 356
Geller, A. M., & Mathieu, R. D. 2012, AJ, 144, 54
Gelman, A., & Rubin, D. B. 1992, StaSc, 7, 457
Gilmore, G., & Randich, S. 2015, Gaia-ESO spectroscopic survey, European Southern Observatory (ESO), doi:10.18727/archive/25
Gilmore, G., Randich, S., Worley, C. C., et al. 2022, A&A, 666, A120
Gokmen, S., Eker, Z., Yontan, T., et al. 2023, AJ, 166, 263
Green, G. M., Schlafly, E., Zucker, C., Speagle, J. S., & Finkbeiner, D. 2019, ApJ, 887, 93
Harris, C. R., Millman, K. J., van der Walt, S. J., et al. 2020, Natur, 585, 357
Hasegawa, T., Malasan, H. L., Kawakita, H., et al. 2004, PASJ, 56, 295
Hourihane, A., François, P., Worley, C. C., et al. 2023, A&A, 676, A129
Hunt, E. L., & Reffert, S. 2024, A&A, 686, A42
Hunter, J. D. 2007, CSE, 9, 90
Hypki, A., & Giersz, M. 2017, MNRAS, 471, 2537
Ibanoğlu, C., Soydugan, F., Soydugan, E., & Dercişoğlu, A. 2006, MNRAS, 373, 435
Irrgang, A., Wilcox, B., Tucker, E., & Schiefelbein, L. 2013, A&A, 549, A137
Jacobson, H. R., Friel, E. D., & Pilachowski, C. A. 2011, AJ, 141, 58
Jadhav, V. V., & Subramaniam, A. 2021, MNRAS, 507, 1699
Joshi, Y. C., Deepak, & Malhotra, S. 2024, FrASS, 11, 1348321

Karagöz, H., Yontan, T., Bilir, S., et al. 2025, AJ, 170, 149
Kharchenko, N. V., Piskunov, A. E., Schilbach, E., Röser, S., & Scholz, R.-D. 2013, A&A, 558, A53
King, I. 1962, AJ, 67, 471
Kobayashi, C., Karakas, A. I., & Lugaro, M. 2020, ApJ, 900, 179
Kobayashi, C., Umeda, H., Nomoto, K., Tominaga, N., & Ohkubo, T. 2006, ApJ, 653, 1145
Koç, S., Yontan, T., Bilir, S., et al. 2022, AJ, 163, 191
Kounkel, M., Covey, K., & Stassun, K. G. 2020, AJ, 160, 279
Kruijssen, J. D. 2014, CQGra, 31, 244006
Lada, C. J., & Lada, E. A. 2003, ARA&A, 41, 57
Leggett, S. K. 1992, ApJS, 82, 351
Leonard, P. J. T. 1989, AJ, 98, 217
Linck, E., & Mathieu, R. D. 2026, AJ, 172, 61
Lindegren, L., Klioner, S. A., Hernández, J., et al. 2021, A&A, 649, A2
Liu, L., & Pang, X. 2019, ApJS, 245, 32
López-Corredoira, M., Cabrera-Lavers, A., Garzón, F., & Hammersley, P. L. 2002, A&A, 394, 883
López-Corredoira, M., & Molgó, J. 2014, A&A, 567, A106
Lu, Y. L., Minchev, I., Buck, T., et al. 2024, MNRAS, 535, 392
Magrini, L., Sestito, P., Randich, S., & Galli, D. 2009, A&A, 494, 95
Magrini, L., Sestito, P., Randich, S., Galli, D., et al. 2017, A&A, 603, A2
Mapelli, M., Sigurdsson, S., Colpi, M., et al. 2004, ApJL, 605, L29
Mapelli, M., Sigurdsson, S., Ferraro, F. R., et al. 2006, MNRAS, 373, 361
Mathieu, R. D., & Geller, A. M. 2009, Natur, 462, 1032
McCrea, W. H. 1964, MNRAS, 128, 147
McLachlan, G. 2000, Finite Mixture Models (Wiley)
McMillan, P. J. 2017, MNRAS, 465, 76
McWilliam, A. 1997, ARA&A, 35, 503
Milone, A. P., Piotto, G., Bedin, L. R., et al. 2012, A&A, 540, A16
Minchev, I., Anders, F., Recio-Blanco, A., et al. 2018, MNRAS, 481, 1645
Minchev, I., Chiappini, C., & Martig, M. 2014, ApJ, 804, L9
Minchev, I., Famaey, B., Combes, F., et al. 2011, A&A, 527, A147
Miyamoto, M., & Nagai, R. 1975, PASJ, 27, 533
Momany, Y., Zaggia, S., Gilmore, G., et al. 2006, A&A, 451, 515
Navarro, J. F., Frenk, C. S., & White, S. D. M. 1996, ApJ, 462, 563
Netopil, M., Oralhan, İ. A., Çakmak, H., Michel, R., & Karatas, Y. 2022, MNRAS, 509, 421
Netopil, M., Paunzen, E., Heiter, U., & Soubiran, C. 2016, A&A, 585, A150
Nissen, P. E. 2004, in in Origin and Evolution of the Elements, ed. A. McWilliam & M. Rauch, 154 (Cambridge Univ. Press)
Nomoto, K., Kobayashi, C., & Tominaga, N. 2013, ARA&A, 51, 457
Otto, J. M., Frinchaboy, P. M., Myers, N. R., et al. 2026, AJ, 171, 91
Pasquini, L., Avila, G., Blecha, A., et al. 2002, Msngr, 110, 1
Pecaut, M. J., & Mamajek, E. E. 2013, ApJS, 208, 9
Pedregosa, F., Varoquaux, G., Gramfort, A., et al. 2011, JMLR, 12, 2825
Plevne, O., & Akbaba, F. 2026, arXiv:2605.23802
Plevne, O., Önal Taş, Ö., Bilir, S., & Seabroke, G. M. 2020, ApJ, 893, 108
Portegies Zwart, S. F., McMillan, S. L. W., & Gieles, M. 2010, ARA&A, 48, 431
Randich, S., Gilmore, G., Magrini, L., et al. 2022, A&A, 666, A121
Ratcliffe, B., Khoperskov, S., Minchev, I., et al. 2025, A&A, 698, A267
Ratcliffe, B., Khoperskov, S., Lee, N., et al. 2026, A&A, 706, A103
Reylé, C., Marshall, D. J., Robin, A. C., & Schultheis, M. 2009, A&A, 495, 819
Ricker, G. R., Winn, J. N., Vanderspek, R., et al. 2015, JATIS, 1, 014003
Riello, M., De Angeli, F., Evans, D. W., et al. 2021, A&A, 649, A3
Robin, A. C., Luri, X., Reylé, C., et al. 2012, A&A, 543, A100
Roškar, R., Debattista, V. P., Quinn, T. R., Stinson, G. S., & Wadsley, J. 2008, ApJ, 684, L79
Schlafly, E. F., & Finkbeiner, D. P. 2011, ApJ, 737, 103
Schönrich, R., & Binney, J. 2009, MNRAS, 396, 203
Sellwood, J. A., & Binney, J. J. 2002, MNRAS, 336, 785
Sinha, A., Zasowski, G., Frinchaboy, P., et al. 2024, ApJ, 975, 89
Sollima, A., Beccari, G., Ferraro, F. R., Fusi Pecci, F., & Sarajedini, A. 2007, MNRAS, 380, 781
Soubiran, C., Cantat-Gaudin, T., Romero-Gómez, M., et al. 2018, A&A, 619, A155
Spina, L., Ness, M., Nordlander, T., et al. 2022, MNRAS, 511, 1217
Spina, L., Ting, Y.-S., De Silva, G. M., et al. 2021, MNRAS, 503, 3279
Taşdemir, S., Çınar, D. C., Canbay, R., et al. 2025, PARep, 3, 1
Taşdemir, S., & Yontan, T. 2023, PARep, 1, 1
Tadross, A. L. 2011, JKAS, 44, 1
Tanık Öztürk, B., Bilir, S., Yontan, T., et al. 2025, AJ, 170, 164
Tarricq, Y., Soubiran, C., Casamiquela, L., et al. 2021, A&A, 647, A19
Taşdemir, S., Elsanhoury, W. H., Çınar, D. C., Haroon, A., & Bilir, S. 2026, RAA, 26, 045016
Tunçel Güçtekin, S., Bilir, S., Karaali, S., Plevne, O., & Ak, S. 2019, AdSpR, 63, 1360
Virtanen, P., Gommers, R., Oliphant, T. E., et al. 2020, NatMe, 17, 261
Viscasillas Vázquez, C., Magrini, L., Casali, G., et al. 2022, A&A, 660, A135
von Hippel, T., Jefferys, W. H., Scott, J., et al. 2006, ApJ, 645, 1436
von Hippel, T., Steinhauer, A., Sarajedini, A., & Deliyannis, C. P. 2002, AJ, 124, 1555
Wiggins, A. I., Quinn, J. R., Oeur, M., et al. 2025, ApJL, 995, L25
Woosley, S. E., & Weaver, T. A. 1995, ApJS, 101, 181
Wu, Z.-Y., Zhou, X., Ma, J., & Du, C.-H. 2009, MNRAS, 399, 2146
Yontan, T. 2023a, AJ, 165, 79
Yontan, T., Bilir, S., Çakmak, H., et al. 2023b, AdSpR, 72, 1454
Yontan, T., & Canbay, R. 2023c, PARep, 1, 65
Yontan, T., Bilir, S., Bostancı, Z. F., et al. 2015, Ap&SS, 355, 267
Yontan, T., Bilir, S., Bostancı, Z. F., et al. 2019, Ap&SS, 364, 152
Yontan, T., Çakmak, T., Bilir, S., et al. 2022, RMxAA, 58, 333
Yontan, T., Bilir, S., Çakmak, H., et al. 2026, arXiv:2608.08216
Zinnecker, H., & Yorke, H. W. 2007, ARA&A, 45, 481